Engineering Structures 353 (2026) 122157

Contents lists available at ScienceDirect

Engineering Structures

journal homepage: www.elsevier.com/locate/engstruct

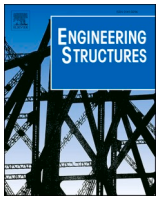

Performance of vector-valued fragility for coastal bridge under earthquake and tsunami hazards

Heng Mei [a,b], You Dong [a,b,*], Dan M. Frangopol [c], Anxin Guo [d,e]

[a] State Key Laboratory of Climate Resilience for Coastal Cities, The Hong Kong Polytechnic University, Hung Hom, Kowloon, Hong Kong, China
[b] Department of Civil and Environmental Engineering, The Hong Kong Polytechnic University, Hung Hom, Kowloon, Hong Kong, China
[c] Department of Civil and Environmental Engineering, ATLSS Engineering Research Center, Lehigh University, Bethlehem, PA, USA
[d] Key Lab of Smart Prevention and Mitigation of Civil Engineering Disasters of the Ministry of Industry and Information Technology, Harbin Institute of Technology, Harbin 150090, China
[e] Key Lab of Structures Dynamic Behavior and Control of the Ministry of Education, Harbin Institute of Technology, Harbin 150090, China

ARTICLE INFO

Keywords:
Seismic-tsunami
Multi-hazard
Tri-variate intensity measure
Isolated bridges
Fragility

ABSTRACT

Extreme hazards such as earthquake and ensuing tsunamis can pose significant threats to offshore infrastructures, among which bridges are particularly vulnerable due to their locations. Accurate assessment of bridge performance under such events is crucial to enhance structural safety. In this study, the fragility method was employed to evaluate bridge capability against combined hazard effects, with three variables introduced to capture multi-hazard intensity. The vector-valued method was used to quantify bivariate tsunami intensities, with different fragility functions compared in their fitting capability. A new fragility form was proposed for earthquake-tsunami scenarios, with the system-level fragility also examined via multiple bridge components. A case study was conducted to compare the effectiveness of various functions to isolated bridges. The component-level fragility shows an inconsistent development with increasing seismic magnitudes but consistent trends with tsunami intensity. The comparison analysis implies the highest fitness of log-sum model, while the proposed method yields consistent outcomes despite the unified factor. System-level fragility results indicate that isolated bridges have notable vulnerability due to multi-component contributions. Further, the expected damage ratio was assessed and shows notable sensitivity to spectral acceleration and relative wave height, as opposed to the limited influences from water depths. This study provides preliminary guidance for estimating the seismic-tsunami fragility of isolated bridges using complex intensity sets.

1. Introduction

Extreme events can cause catastrophic impacts on infrastructure. Among these, earthquakes pose a significant threat to offshore bridges owing to their potentials in triggering tsunamis. Most offshore bridges adopt isolated configurations due to their convenient construction, with shear keys used along with bearings to support and restraint superstructures. In recent decades, many cases of bridge damage and failure have been reported, such as in Chile (2010) [1,2] and Japan (2011) [3], with such isolated layouts also found to protect critical components given proper design [4,5]. Such hazards tend to pose serious threats to transportation and community safety in coastal areas [6–10], and thus leads to the necessity to provide reliable evaluation on bridge performance under such hazards.

Earthquake and tsunami hazards are highly uncertain in both occurrence and intensity. For a specified seismic-tsunami event, the bridge performance can be evaluated using the fragility method. Such method has proven effective toward individual hazards such as earthquakes [11] and hurricanes [12]. Normally, fragility formulas were expressed using normal or lognormal distributions, and the generalized linear model (GLM) was also widely adopted. In this regard, individual intensity measure (IM) has been widely used while the performance of bivariate and multi-variate IMs was rarely investigated yet. Gehl et al. [13] studied seismic bridge fragility and found that incorporating multiple IMs can enhance accuracy by reflecting more seismic characteristics. Alam et al. [14] investigated the fragility of bridges subjected to hurricane-induced extreme waves. Their study indicated that using multiple IMs such as water depth in addition to the wave height can

* Corresponding author at: State Key Laboratory of Climate Resilience for Coastal Cities, The Hong Kong Polytechnic University, Hung Hom, Kowloon, Hong Kong, China.
E-mail address: you.dong@polyu.edu.hk (Y. Dong).

https://doi.org/10.1016/j.engstruct.2026.122157
Received 17 August 2025; Received in revised form 29 December 2025; Accepted 10 January 2026
Available online 23 January 2026

provide better evaluation on bridge performance, again highlighting the benefit of using multi-variate IMs. Similar findings were also available with respect to other individual hazards [15–17].

In recent years, an increasing number of multi-hazard events were reported, underlining the demand to expand fragility estimation from single to combined hazard effects. In this regard, many studies have been conducted by focusing on various hazard combinations. These hazards can be classified into correlated (e.g. earthquake-tsunami, hurricane-wave) and independent (e.g. earthquake-corrosion, earthquake-scour) categories. And fragility method is also feasible and employed in this context. Guo et al. [18,19] conducted studies to investigate the time-variant fragility of bridges under combined scour-earthquake effects, implying an escalated fragility level with prolonged operation periods. Li et al. [20] investigated the seismic fragility under corrosion effects and found the increasing fragility due to a declined resistance. Argyroudis et al. [21] addressed the fragility of transportation system under multi-hazard scenarios by considering both geotechnical and climatic hazards.

While combined with long-term hazard, the hazard causing direct impacts is often defined as demand terms, with long-term effects correlating to structural capacity to reflect strength deteriorations. Typical examples are earthquakes in conjunction with scour and corrosion effects [20,22]. Whereas under correlated hazards, the secondary hazard serves as the demand factor while the primary hazard is deemed as capacity to account for the deterioration, as reported in earthquake-tsunami and earthquake-landslide events [23,24]. In contrast, both hazards should be included as demand terms within concurrent scenarios, with structural capacity defined according to merely their initial states. Consequently, it is essential to incorporate multi-hazard intensities based on their demand and capacity under characteristic hazard actions.

To this regard, the vector-valued method has been proposed and used for seismic analysis. Hu et al. [25] examined the seismic fragility of slopes using both scalar- and vector-based fragility functions, suggesting the likelihood of distorted fragility estimation by scalar methods. Guo et al. [26] inspected the subway station fragility under local earthquake hazards by considering both concrete and soil damages. The optimal intensity measure was determined by comparing distinct vector-valued combinations, with the result also showing misestimation from scalar functions. Besides, Bojórquez et al. [27] applied such method to steel frames and found the dependence of vector function upon seismic inputs. While such method has been long used in seismic study, their applicability to multi-hazard events are limited yet [28], and the effectiveness of vector functions remains unclear.

To this end, this study focused on the seismic-tsunami fragility of bridges using a vector-valued approach, with various vector functions compared in their fitting capability. Besides, a vector function was developed to underline sequential impacts of earthquake and tsunami [29]. The performance of vector-based method on system-level fragility was examined, with second-order-limit-method (SOLM) used to incorporate multi-mode failure of bridge girders. The fragility was converted to damage ratio to quantify the damage severity induced by such cascading hazards. A case study was performed to typical coastal isolated bridges. The pier fragility was found to increase with seismic intensity at lower tsunami levels, but shows a reverse trend at higher tsunami level. In contrast, the girder fragility increases consistently with both hazard intensities. The fragility of bearings and constrainers remains stable for different damages states. The comparison among vector functions indicates that the log-sum formula can achieve the highest accuracy, while the square-root and log-poly-2 models give higher and lower estimation, respectively. The proposed function yields acceptable prediction but tends to overestimate at the upper bound. The system-level fragility was calculated for the best vector model, showing the limitation of vector-based method in capturing the systematic performance of isolated bridges under. Furthermore, the damage ratio demonstrates the development of remaining structural performance under different intensity baselines.

The main contents are organized as follows: (1) Section 2 describes the procedures for estimating seismic-tsunami fragility in both component and system levels; (2) illustrative case study is performed in Section 3 by considering hazard and structural uncertainties; (3) Section 4 discusses the results of statistical and analytical fragility, and the comparison is made among different vector-valued functions; (4) concluding remarks were presented in the last section.

2. Methodology for assessing seismic-tsunami fragility

To evaluate the performance of coastal bridges under sequential seismic-tsunami hazards, the fragility method was adopted in the present study, for which intensity measures are required for both hazards, along with fragility function able to quantify typical multi-hazard impacts. In addition, the system-level fragility was calculated to integral various component contributions to complete bridge functionality.

2.1. Selecting hazard intensity and qualitative correlation

Selecting appropriate hazard IMs and accurately estimating uncertainties are essential for evaluating bridge performance under catastrophic events. The current study emphasized the magnitudes of earthquake and tsunami, as well as their interdependence. In view of preceding studies, a number of IMs have been proposed for the seismic fragility estimation, such as peak ground acceleration (PGA), velocity (PGV), displacement (PGD), spectral acceleration (S_a), and Arias intensity (I_a), while cumulative IMs such as cumulative absolute velocity (CAV) was also employed in many cases [30]. In this context, the selected IM should comply with the dominant structural responses to ensure a strong correlation between hazard impacts and structural reactions. Hence, spectrum levels (S_a) were chosen here for earthquake hazards due to the sensitivity of isolated bridges to shaking frequencies [31], as illustrated in Fig. 1**(a)**.

The bridge fragility under tsunamis have also been investigated in many research. Unlike seismic loads that dominate in the horizontal direction, tsunami forces can act in multiple directions with diverse magnitudes, as shown in Fig. 1**(b)**. Girders and piers are the primary component subjected to tsunami loads, and the force on girders is sensitive to the water level [32]. In this context, tsunami loads consist of hydrostatic and hydrodynamic components, which results from unbalanced pressure and the flow velocity, respectively. Among the governing factors of tsunami impacts, wave heights have dominant influences [33] while water depths also play an essential role by affecting the immersed condition and then the distribution of tsunami loads [23,34]. Hence, a bivariate form intensity measure was specified as (H,d) to highlight the multi-direction tsunami load effects. And the wave height parameter is further normalized as $(\varepsilon = H/d)$ to discern the contribution of wave height at different water depths.

Earthquake and trigerred tsunamis are complex in their correlations. Prior research implies an inverse development of seismic intensity with epicenter distances [35], and tsunami intensity was found to also depend on the travelling length. Fig. 2 illustrates their correlations conditional on different epicenter scale, where SWL refers to still water level and $wd_1 \sim wd_3$ are representative to the water depth at different locations, including onshore areas (wd_1), moderate-depth areas (wd_2), and inshore areas (wd_3). Given long distance between rupture and the bridge site, both hazard intensities tend to decreases as the distance further increases owing to the attenuation effects (Fig. 2**(b)**). However, tsunami intensity can also increase with distance when the initial value is considerably small (inshore water), as the disturbed water volume rises while seismic intensity again exhibits decline trends (Fig. 2**(a)**). Accordingly, the intensity of tsunami hazard becomes less sensitive to the changing water depth in onshore areas because water level remains stable at such point. In the current research, a long-distance case was used in line with most mega-tsunami observed in past decades [36],

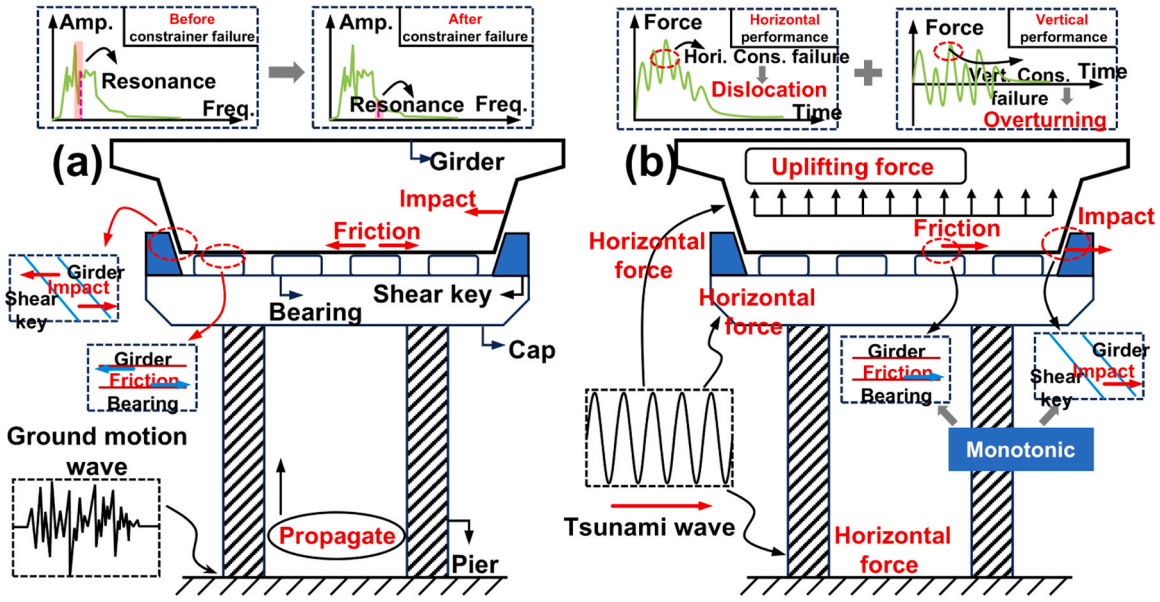

Fig. 1. Correlation between structural response and hazard impacts for isolated bridges under: (a) earthquakes; (b) tsunamis.

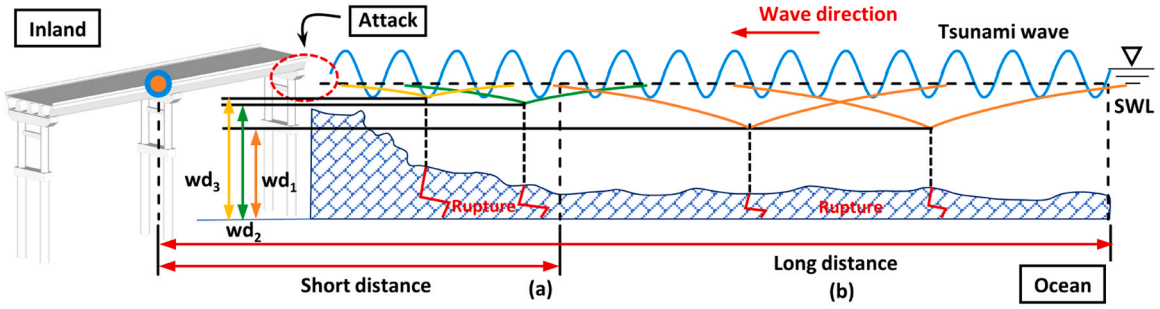

Fig. 2. Mechanism of intensity development for successive earthquake-tsunami hazards subject to: (a) short distance; (b) long distance.

leading to positive earthquake-tsunami correlations.

As a follow up, the correlation within the bivariate tsunami IMs was also evaluated under different distances. In this case, water depth and wave heights are inversely correlated at larger distances, because the dispersion has dominant effects conditional on adequate space for shoaling development [37]. By contrast, they are positively correlated at a shorter distance because of the rapidly growing wave height also due to shoaling effects. Accordingly, a positive correlation was employed in this study alongside the long-distance assumption, with an inverse correlation adopted for the intra-dependence of the bivariate tsunami IMs. Note that the same intensity measures are feasible in the short-distance case, whereas correlation needs to reverse to avoid biased estimation of bridge fragility.

2.2. Calculating multi-hazard fragility

In this study, the lognormal fragility function was used to identify the bridge performance under sequential seismic-tsunami hazards. The analytical fragility for individual hazards can be denoted by the following equation,

$$P(LS \geq LS_i | IM = im) = \Phi\left(\frac{\ln(im) - \mu_{\ln IM|LS_i}}{\sqrt{\sigma^2_{\ln IM|LS_i} + \sigma^2_{\xi}}}\right) \quad (1)$$

where μ_{LS_i}, σ_{LS_i} are the mean and variance at i-th limit state (LS), while σ_{ξ} accounts for the structural uncertainty. Each parameter can be obtained via regression analysis to the statistic fragility results [38]. In this study, the limit states of bridge components were defined as per Table 1, with four primary components reckoned according to the functionality of isolated bridges. Here, the four limit states of girder are defined as [34], D1 = closest distance from shear key bottom vertex to bearing edge; D2 = distance from shear key vertex to outmost bearing center; D3 = distance from shear key vertex to the inner edge of outmost edge; and D4 = distance from girder mid-line to outmost pier cap edge. Besides, W is defined as the distance of centreline of adjacent box girders.

Table 1
Componential limit states of isolated bridges.

Component	Demand parameter	Limit states				Reference
		LS_1	LS_2	LS_3	LS_4	
Pier	Drift ratio (-)	0.007	0.011	0.07	0.03	Siqueira et al. [39]
Girder	Horizontal dislocation (mm)	D1	D2	D3	D4 +W/2	Mei and Guo [23]
	Vertical uplifting (mm)	N/A	N/A	N/A	H_{sk}	Mei et al. [28]
Bearing	Shear strain (%)	100	150	200	250	Zhang et al. [40]
Shear key	Deformation (mm)	δ_y	$7\delta_y$	$14\delta_y$	$22\delta_y$	Zakeri et al. [41]

Notes: δ_y denotes the yield deformation of RC shear keys [34], H_{sk} denotes shear key height.

Earthquake and tsunami can cause typically successive impacts to coastal bridges. Hence, their intensities were treated separately while formulating capacity and demands terms in the multi-hazard fragility function. In this context, tsunami hazards often follow the initial seismic events, with a delay from minutes to hours depending on travelling length. During such events, coastal bridges sustain the initial damages under seismic actions, and then experience extensive deterioration under ensuing tsunami loads. The initial seismic level can affect not only the tsunami performance of bridge, but also the structural uncertainty under the secondary tsunami impacts. Hence, the seismic IM was included in both capacity and variance terms using a polynomial formula [23,28].

To accommodate the bivariate tsunami IMs, a vector-valued fragility function was adopted to reflect the intra-dependence. Several vector fragility functions were introduced according to the correlation analysis in Section 2.1, see Table 2. Herein, IM_1, IM_2 denote the two intensity measures for tsunami hazards while X refers to the vector-valued IM. Parameter γ was adopted to account for complementary effects of relative wave height (H/d) and water depth (d), with another independence state represented by a, b, c (log-poly-1) and $a_1 \sim a_2, b_1 \sim b_2$ and c, d in log-poly-2 model. And the same principle also applies to the proposed square-root method. The first one shows the inverse correlation between water depth and wave height, while the second one introduces a constant c. The third formula introduces second-order terms and the production to reflect their interference. In addition, the two proposed formulas calibrate the different scales of relative wave height (0–0.7) and water depth (meters) by including constant c. In addition, the square operation in models 4 and 5 is introduced to ensure positive results for square-root calculation, while the unified form was adopted to underline their interdependences.

To evaluate the effectiveness of various vector-valued functions, the AIC principle was employed by considering both model complexity and prediction errors [14], which takes the general form as follows

$$AIC = 2k + D \tag{2}$$

where k is the number of parameters in models, and D is the statistic deviance involving prediction errors. By comparing the predicted and statistical fragility, the error can be estimated using the following equation,

$$D = 2\sum_{j=1}^{m}\left[y_j \ln\left(\frac{y_j}{\widehat{\mu}_j}\right) + \left(n_j - y_j\right)\ln\left(\frac{n_j - y_j}{n_j - \widehat{\mu}_j}\right)\right] \tag{3}$$

Note that y_j is the occurrence number at a specified intensity of single hazard, or combined effects in multi-hazard cases. $\widehat{\mu}_j$ denotes the estimated occurrence number. n_j refers to the total calculation number for each hazard level, while m represents the total interval number across overall hazard intensities.

2.3. Evaluating system-level fragility

Isolated bridges are comprised of different components that operate together to ensure the bridge functionality. Therefore, each component damage can possibly contribute to bridge paralysis or even failures. Therefore, system-level fragility was used here to compare the applicability of various vector-valued models. In this study, the second-order limit method (SOLM) [43] was used to account for the complex components in isolated bridge, see Eq. 4. Note that such method was initially proposed for estimating the failure probability, but is also utilized here for other limit states.

$$P_{f,1} + \sum_{i=2}^{m}\max\left(P_{f,i} - \sum_{j=1}^{i-1}P_{f,ij}, 0\right) \le p_{f,\text{system}} \le \sum_{i=1}^{m}P_{f,i} - \sum_{i=2}^{m}\max_{j<i}\left(P_{f,ij}\right) \tag{4}$$

In Eq. 4, $P_{f,i}$ is the exceedance probability of i-th component, while $P_{f,ij}$ denotes the coincident occurrence of i- and j-th components. Note that the narrow bound was attained by evaluating all combinations due to the indeterministic sequence of distinct components. As Eq. 4 is subject to only single failure pattern for each component, the original expression needs to be reformulated given multiple failure modes. Prior study has shown that the girder element in isolated bridges is prone to both uplift and swash-away failures during tsunamis, in addition to unseating under earthquakes. Hence, the original SOLM can be updated as,

$$\begin{aligned} p_{f,system} \ge (1-\delta)\cdot P_{f,1} + \delta\cdot\max\left(P_{f,1}^{unseat}, P_{f,1}^{uplift}\right) + \\ \sum_{i=2}^{m}\max\left((1-\delta)\cdot P_{f,i} + \delta\cdot\max\left(P_{f,i}^{unseat}, P_{f,i}^{uplift}\right) - \sum_{j=1}^{i-1}P_{f,ij}^{*}, 0\right) \end{aligned} \tag{5}$$

$$p_{f,\text{system}} \le \sum_{i=1}^{m}\left[(1-\delta)\cdot P_{f,i} + \delta\cdot\max\left(P_{f,i}^{unseat}, P_{f,i}^{uplift}\right)\right] - \sum_{i=2}^{m}\max_{j<i}\left(P_{f,ij}^{*}\right) \tag{6}$$

$$\begin{aligned} P_{f,ij}^{*} = \delta\cdot P\left[\max\left(DS_i^{unseat}, DS_i^{uplift}\right) = ds_k, DS_j = ds_k\right] + \\ (1-\delta)\cdot P\left[DS_i = ds_k, DS_j = ds_k\right] \end{aligned} \tag{7}$$

in which $P_{f,i}^{unseat}, P_{f,i}^{uplift}$ are the probability of unseating and uplifting failures for girder element. δ is the dummy index equal to 1 and 0 for girders and other components, respectively. Besides, $P_{f,ij}^{*}$ is the concurrent failure probability of components i and j, with the dummy notation also included. Moreover, the maximum operator was used to account for the dominant failure mode, which represents a strong time-dependent failure sequence of uplifting followed by swashing away of girders. While this might provide underestimated results, it is reckoned reasonable as significant horizontal and vertical girder movements often occur concurrently.

3. Case study

Based on the component- and system-level fragility defined above, the case study was demonstrated in this section. Begin with the basic information of prototype bridge, characteristic loads from earthquake and tsunami event are estimated, with fiber-based finite element models developed using OpenSees. Besides, uncertainty sources were assigned to hazard actions and structural characteristics through sampling methods.

Table 2
Expressions of vector-valued fragility functions.

No.	Type	Expression	Parameters to be determined	Reference
1	Log-sum	$\ln X = \gamma \ln IM_1 + (1-\gamma)\ln IM_2$	γ	Mei et al. [28]
2	Log-poly-1	$\ln X = a \ln IM_1 + b \ln IM_2 + c$	a, b, c	Jafarian and Miraei [16]
3	Log-poly-2	$\ln X = a_1 \ln IM_1 + b_1 \ln IM_2 + a_2(\ln IM_1)^2 + b_2(\ln IM_2)^2 + c \ln IM_1 \ln IM_2 + d$	a_1, b_1, a_2, b_2, c, d	Modica and Stafford [42]
4	Square-root-nounify	$\ln X = \sqrt{a(\ln c + \ln IM_1)^2 + b(\ln IM_2)^2}$	$a, b > 0$	This study
5	Square-root-unify	$\ln X = \sqrt{\gamma(\ln c + IM_1)^2 + (1-\gamma)(\ln IM_2)^2}$	$\gamma \in [0,1]$	This study

3.1. Description of prototype bridge

In this study, a representative prototype was developed according to a featured segment of sea-crossing viaducts, which encompasses three-span simply-supported girders with box-shaped girders. This enables a realistic assessment of isolated bridge under earthquake-tsunami hazards through detailed component-level modeling.

3.1.1. Design information of bridge

Fig. 3 illustrates the geometric layout and component details of the bridge case. The side span takes 30 m in length while the middle span is extended to 40 m. The bridge girder was continuous and cross the entire bridge span, with the section also detailed in this figure. The bridge pier consists of two columns with circular section, along with a linkage beam in the middle. The pier column is 1.5-m in diameter and 8.5-m in height, and was reinforced with 40 × Φ25 core rebar. The pier was constructed using C35 concrete ($f_{cu,k}$ = 35 MPa) and HRB 400 steel (f_y = 400 MPa). The isolation between super- and sub-structures was achieved via rubber bearings, along with RC shear keys for extra restraints. Rubber bearings were designed with 300-mm width, 500-mm length, and 100-mm height. RC shear keys adopt a monolithic interface and was designed as per Mei and Guo [44]. The bridge pier adopted a robust design to ensure sufficient resistance both horizontally and vertically. In contrast, the girder element was built with C30 concrete ($f_{cu,k}$ = 30 MPa).

3.1.2. Earthquake and tsunami load modelling

Earthquake and tsunami often impact bridges successively. As the time interval between hazards depends on epicenter distance, their coincident effects were neglected, and the coupling effect when shaking bridges interact with water was also beyond the scope of this research. Isolated bridges have complex dynamics under earthquakes due to separated connection between girder and piers. Nonlinear linkage element such as bearings, shear keys can further enhance their sensitivity to seismic frequency contents due to isolated configurations. Besides, the discontinuous state between girder and piers can further alters bridge dynamics by enlarged natural periods. Hence, natural seismic records were used in this study, with 15 records selected by matching the S_a value at first-order natural period T_1 = 1.36 s. And the record database was referenced to Baker and Lee [45], with original records scaled and ranging from 0 to 2.0 g with a 0.2-g interval. Notably, inland records with major short periods were employed to cope with the relatively small periods of the examined bridge, though submarine records often encompass significant long-period segments.

Tsunami intensities are essentially correlated with seismic levels, but are also affected by other factors such as seashore topography and water depth. Simulation method can well capture this but has rather high computational demand, making it unsuitable for fragility analysis. Therefore, the two hazards were treated separately in this study for the joint fragility calculation, leading to a maintained pattern of tsunami force at each seismic level. On this basis, tsunami forces on bridges was estimated as per Huang et al. [46] for box girders, which consist of horizontal and vertical components as follows,

$$\begin{cases} F_V = \Delta F_{hv} + F_{v,dyn} \\ F_H = \Delta F_{hd} + F_{h,dyn} \end{cases} \tag{8}$$

in which F_V, F_H are vertical and horizontal components, ΔF_{hv} is the static vertical load defined as buoyancy along with overtopping water weight. ΔF_{hd} denotes the static force difference between front and back sides of girders. Besides, $F_{v,dyn}$ and $F_{h,dyn}$ represent dynamic effects in corresponding directions. Specifically, the static components ($\Delta F_{hv}, \Delta F_{hd}$) are dependent on water elevation, while dynamic tsunami loads ($F_{v,dyn}$, $F_{h,dyn}$) mainly involve with flow speeds in vertical and horizontal directions. More details in this regard can be traced to Mei and Guo [34]. The tsunami force on bridge piers was estimated using Morison equation [47] as Eq. 9, in which C_D is drag coefficient, and ρ, g are mass density (kg/m^3) and gravity acceleration (m/s^2). u_x denotes the horizontal velocity (m/s) that also plays an important role in developing horizontal dynamic impacts ($F_{v,dyn}$).

$$F_p = 0.5\rho g u_x |u_x| C_D \tag{9}$$

To model the tsunami development close to bridge sites, solitary wave model was used to derive major flow properties [48,49]. Such method has proven effective in capturing the high nonlinearity of tsunami waves in shorelines [33]. The bivariate tsunami IMs also matches with solitary waves as they rely on relative wave heights (H/d). In this context, H/d was scaled in steps of 0.05, ranging from 0 to 0.7 to account for the breaking limit [50]. Note that overturning effect was neglected in this study due to large deck widths and consequently enormous self-weight and resistant moments. Anothe reason is that

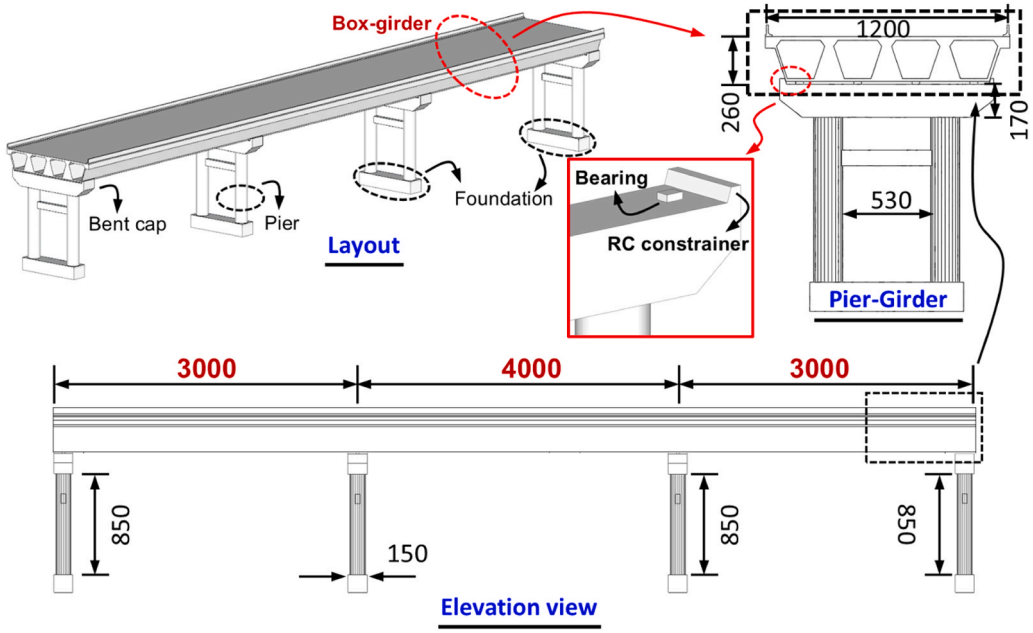

Fig. 3. Geometry arrangement and detailed configuration of inspected bridge (Unit = cm).

damming water often occurs prior to tsunami arrivals, limiting the unbalanced vertical impacts that further induces moment effects. Further, shoaling effects that give more accurate wave conditions are excluded by focusing on isolated bridge performance.

3.2. Finite element modelling

In this study, OpenSees program was employed to perform structural analysis under combined seismic-tsunami impacts. The numerical bridge model was developed in Fig. 4, with girders modeled using an integral elastic beam-column element without breaks. In contrast, the double-column pier was modeled by nonlinear beam-column elements, with fiber sections defined by Concrete01 and Steel02 materials. On this basis, the strength of core concrete was calculated by considering the confinement effects from transverse rebar [51].

By contrast, the linkage component was modeled using zero-length elements to address predominant shear effects. The rubber bearing was defined with elasticPP material, with stiffness and strength set to 2143 kN/mm and 20 kN, respectively. Shear key elements were denoted by combining Pinching4 and ENT materials to accommodate compression-only behavior, with the parameters determined as per Mei and Guo [34]. On this basis, rigid link was assigned to girder and pier nodes to ensure coordinated movements, with fixed boundary applied at pier base to model sufficient constraints. Thus, structural analyses were performed along with incremental dynamic analysis (IDA) and SOLM methods.

3.3. Uncertainty estimation

To account for the uncertainty in structural capacity (Eq.1), we adopted a number of random distributions for major parameters, as outlined in Table 3. The geometry parameter was incorporated only for bridge piers, while strength parameter was applied to other components. Concrete density uncertainty was defined byt the ratio about standard density value at $\rho_{std} = 2.65$ t/m^3. Note that the interdependence among parameters was neglected in this study. Random sampling was performed to capture the structural uncertainty, along with a random matching method to reduce repeated seismic analysis [28]. Such method implements only one record matched for each bridge model across each scaling level of seismic intensity. And it also requires each record selected at least once to account for uncertainties from record to record. Seismic-tsunami analysis was then conducted to attain bridge responses and fragility results. In this context, Latin-Hypercube-Sampling (LHS) technique was used to generate even distributed bridge parameters, with the sampling number set to 100 in this study. By combining 14 relative wave height (H/d) and depth (d) scaling levels with 10 spectrum level (S_a), totally 1.96×10^5 rounds of simulation were conducted on 40-core CPUs.

4. Discussion on results

This section presents a comprehensive discussion on the analysis results of multi-hazard fragility and risk assessment. Both component- and system-level results are examined, focusing on sequential earthquake-tsunami influences and vector-valued model performance.

4.1. Empirical component-level fragility

In this study, a statistical fragility analysis was first adopted to assess bridge performance under combined hazard effects. Initially, the fragility of individual bridge components was estimated for each hazard independently, followed by a joint fragility across different hazard baselines.

4.1.1. Fragility under individual hazard

Fig. 5 displays the stepwise seismic fragility of major components, using the first span as an example. All components show increasing fragility with S_a up to 1.2 g, though the trend varies at higher seismic levels. As shown in Fig. 5**(a)**, the probability of slight damage increases consistently with seismic intensity, whereas that of moderate and severe damages exhibit non-monotonic trends. Notably, moderate-damage fragility decreases at higher intensities, while extensive- and severe-damage fragility shows consistent growth. This occurs because the initial moderate-severe range (LS_2~LS_4) responses progress to extensive state (LS_3) when S_a rises. By contrast, other responses decline to slight damage (LS_1), reducing the fragility at moderate damage but increasing

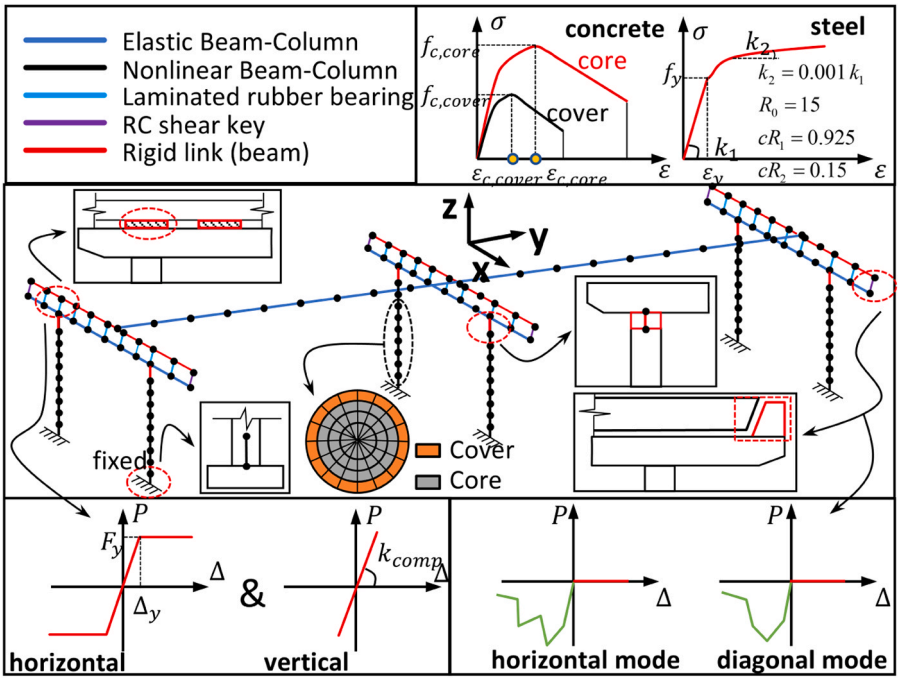

Fig. 4. Details of numerical bridge model in OpenSees program.

Table 3
Information of random distribution for structural uncertainty.

Component	Parameter name	Notation	Unit	Distribution	Parameters		Reference
					1	2	
Pier	Column diameter	D	m	Normal	1.5	1.45	This study
	Rebar diameter	d_s	mm	Normal	25	2.0	
	Concrete strength	$f_{cu,k}$	MPa	Normal	35.0	4.0	
	Rebar strength	f_y	MPa	Lognormal	5.99	0.01	
Girder	Elastic modulus	E	GPa	Normal	30	0.2	
Bearing	Shear modulus	G_{bear}	MPa	Uniform	0.66	2.07	AASHTO [52]
	Friction coefficient	μ	N/A	Lognormal	-0.92	0.1	Zakeri et al. [41]
Shear key	Peak strength	f_{sk}	kN	Normal	1921	50	Mei et al. [28]
	Peak deformation	δ_{sk}	mm	Normal	13.03	2.2	
Others	Normalized mass density	ρ/ρ_{std}	N/A	Uniform	0.9	1.1	Nielson and DesRoches [53]
	Damping ratio	ξ	N/A	Normal	0.045	0.0125	Bryant [38]

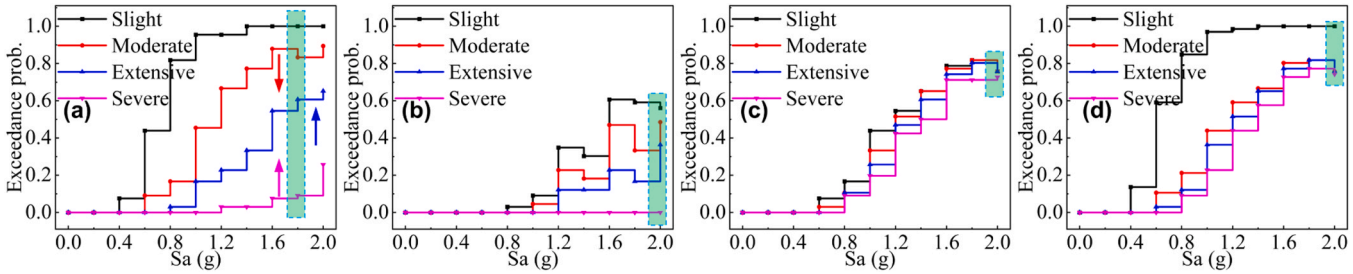

Fig. 5. Statistic seismic fragility of bridge components: (a) pier; (b) girder; (c) bearing; (d) shear key.

the fragility of higher damage levels (LS_3-LS_4).

Girder fragility shows a two-stage pattern for slight to extensive states (LS_1~LS_3), with negligible fragility at severe damage across all seismic intensities, as seen in Fig. 5**(b)**. This suggests adequate resistance of superstructure to individual seismic loading. Such trend was also found at $S_a = 2.0$ g, where moderate- and extensive-damage fragility increases while severe-damage fragility decreases slightly. The fragility of bearing and shear key increases consistently for $S_a < 2.0$ g but decreases at 2.0 g, because significant pier damage reduces the transferred force and protects isolated elements, as shown in Fig. 5**(c)-(d)**.

The following analysis examined the tsunami performance of bridges without discerning prior seismic load magnitudes, for which a representative water depth was selected at 8.5 m, as shown in Fig. 6. The result shows that tsunami fragility differs from seismic result in Fig. 5, where pier fragility increases steadily with H/d, but then with a sharp rise at H/d = 0.45 (Fig. 6**(a)**). The severe-damage fragility reaches 0.78 at the upper bound, reflecting strong multi-direction tsunami forces. The fragility of girder component increases for H/d < 0.45 across states, but then declines for H/d ≥ 0.50, see Fig. 6**(b)**. This can be attributed to the pier collapse while sustaining major $P-\Delta$ effects [34], which then reduces the likelihood of girder unseating failures. Specifically, tsunami loads act on girder both vertically and horizontally, with horizontal effect pushing girder away from initial position, i.e. unseating failure. In contrast, vertical loads can apply both downward and upward, leading to swash-away failure subject to upward effects but notable compressions in downward cases. Such compressive effects can combine with horizontal loads and result in significant $P-\Delta$ effects, especially when coupled with residual seismic deformation. Linkage components also follow similar trends and exhibit minimal difference among distinct damage states, as shown in Fig. 6**(c)-(d)**.

To capture cascading effects, tsunami fragility was then analyzed considering prior seismic damages. To this regard, several prior seismic magnitudes were selected at 0.2, 0.8, 1.4 g, and the conditional fragility was assessed by dividing the exceedance of sample number (n) over all sampling number (14 H/d levels×100 structural samples = 1400 cases) given the same initial S_a value, as shown in Fig. 7. Though the water depth was specified at 8.5 m for illustration, similar conclusion can be drawn for other water levels. Note that only residual seismic response was considered here but neglecting the peak value during earthquakes. For $S_a = 0.2$ g, all initial fragility at H/d = 0 is zero for overall components, implying negligible residual damage due to initial earthquakes. The girder fragility remains zero even at $S_a = 0.8$ g, coinciding with the rare seismic fragility in Fig. 5. Pier fragility shows a sudden growth at H/d = 0.45, aligning also with the case ignoring earthquake intensities (Fig. 6). In comparison, pier fragility at $S_a = 1.4$ g increases gradually across tsunami levels, with severe-damage fragility slightly

decreasing at H/d = 0.6, as seen in Fig. 7**(a3)**. The major reason lies in the different combination of vertical and horizontal wave loads under

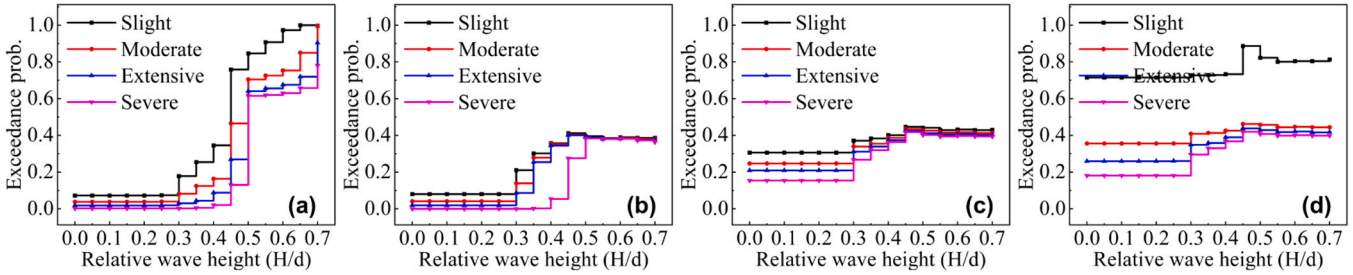

Fig. 6. Statistic tsunami fragility of bridge components across seismic intensity (d = 8.5 m): (a) pier; (b) girder; (c) bearing; (d) shear key.

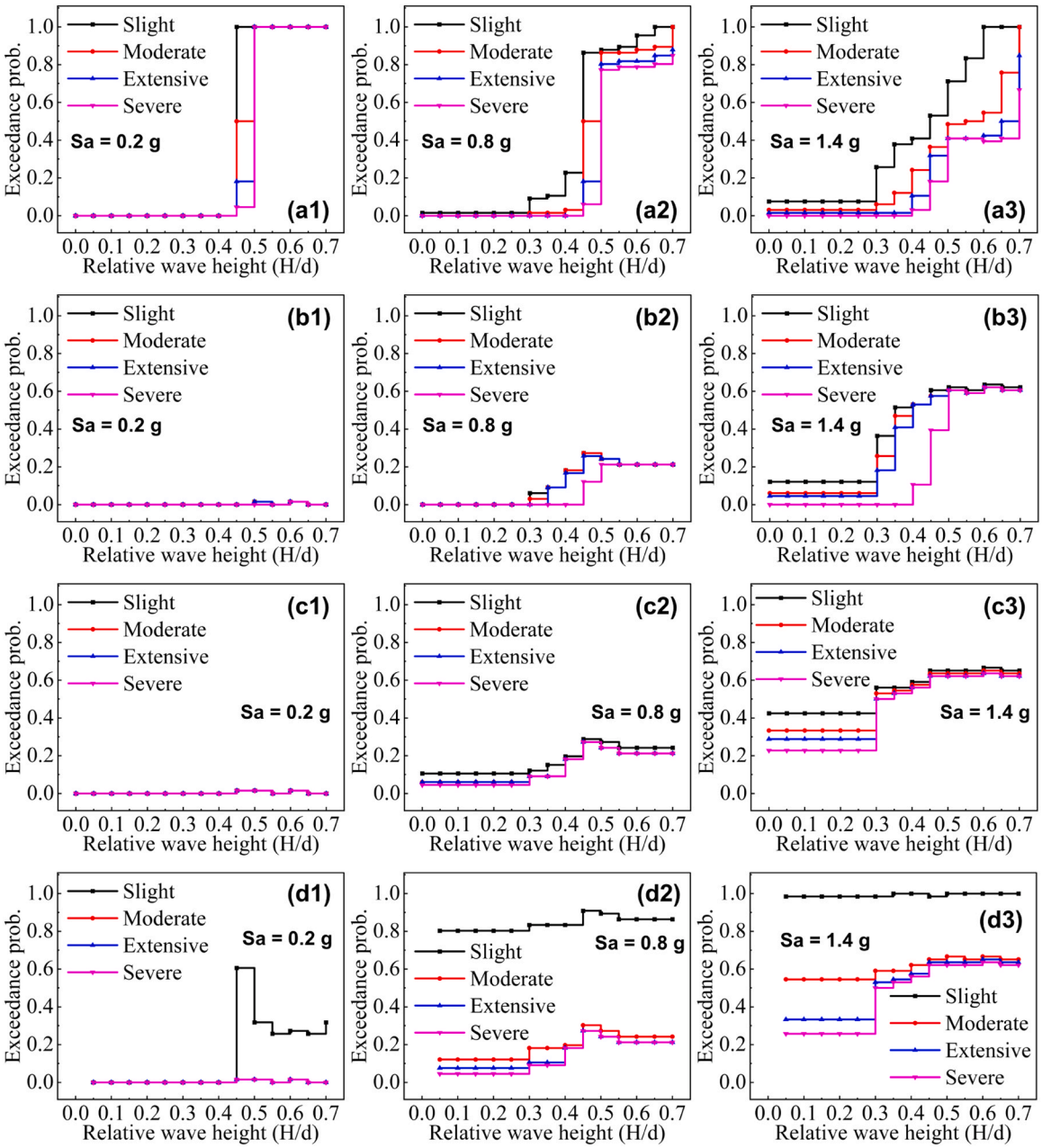

Fig. 7. Statistic tsunami fragility of bridge components after different intensities of earthquakes (d = 8.5 m): (a) pier; (b) girder; (c) bearing; (d) shear key.

varying H/d amplitudes. In details, horizontal loads dominate at H/d = 0.6 and result in essential pushing effects on bridge girders, inducing significant swashing failure of girders and decreasing the pier fragility. In contrast, vertical loads substitute at larger H/d values and lead to pier collapses via extensive P-Δ effects. As a result, the fragility value follows a rise-decline trend in Fig. 7 **(a3)**. Moreover, such result barely applies to 0.2 and 0.8 g because of different residual seismic damages.

For girder and bearing in Fig. 7**(b1), (c1)**, their fragility is near zero at S_a = 0.2 g, showing limited impacts from weak earthquakes even followed by strong tsunamis. At higher seismic levels, fragility was found to initiate at lower H/d thresholds of 0.5 and 0.45 for girder and bearing, respectively. Again, pier fragility was essential in this case while few damages were observed for the linkage elements. Shear key fragility follows similar patterns, except for slight damage (LS_1) that corresponds to 10.07-mm (yield) deformation. In addition, girder fragility at H/d = 0 remains zero until S_a = 1.4 g while bearing damage starts from 0.8 g (Fig. 7**(b)**), highlighting the influence of residual damages due to rising seismic levels. The tsunami fragility of linkage elements also shows prompt increases with enhanced seismicity, implying notable decline in bridge resistance due to prior earthquake. However, such fragility remains steady near the upper bound due to dominant pier failures, as implied in Fig. 7**(a2)**. Fig. 7**(b2)** indicates an increasing girder fragility for severe damage compared to the decline for other states at H/d > 0.5, because the original damage of LS_1~LS_3 progresses to severe levels. In contrast, the calculated fragility exhibits declined trends for both shear keys and bearings, implying the dominance of pier collapse failure modes due to $P-\Delta$ effects, as seen in **(c2)** and **(d2)**. Due to the same reason, pier fragility undergoes significant growth across all prior seismic intensities, as seen in Fig. 7**(a)**.

Therefore, pier elements in isolated bridges suffers significant fragility under both seismic and tsunami hazards. By contrast, isolation devices can effectively protect superstructures by sacrificing (shear keys) and plastic deformation (bearings), leading to the minimal

fragility of girders subject to low-level initial earthquakes. However, it also develops with seismic magnitudes due to diminishing constraints from damaged isolated devices.

4.1.2. Fragility under multi-hazard actions

Building on the individual hazard fragility, the joint fragility under successive earthquake-tsunami impacts was evaluated for pier and girders. Herein, analysis was performed for three baseline parameters: water depth (d), relative wave height (H/d), and spectral values (S_a). Fig. 8 shows the joint fragility at a fixed water depth of 8.5 m. The pier fragility rises monotonically with H/d across all damage states (LS_1~LS_4). However, a decreasing trend with rising seismic intensity was observed at large H/d values for moderate to severe damage states, see **(a2)-(a4)**, with slight-damage fragility maintaining steady at unity across most S_a-H/d ranges. Here, the slight-damage fragility increases steadily with S_a, as opposed to the severe-state fragility that decreases at higher S_a, again owing to the absence of shear key constraints after initial earthquakes.

Compared with piers, girders show lower fragility and smaller maximum value below 0.8 (Fig. 8**(b)**). An up-down trend with increasing H/d values is observed across all spectral values for slight to severe damage states, with the transition point (peak) occurring at H/d = 0.45. In comparison, the development of girder fragility increases stably at lower S_a levels but then becomes inconsistent at higher seismic levels. While subjected to lower seismicity, girder fragility remains near zero despite tsunami magnitudes, which again underscores the role of significant seismic damages in escalating tsunami vulnerability. In addition, girder fragility also exhibits an up-down trend owing to the absence of shear key constraints.

Fig. 9 presents the joint fragility at a constant H/d of 0.35. In this case, pier fragility rises with S_a across all damage states except moderate (LS_2), which declines at $S_a = 1.8$ g as the damage shifts toward slight state (LS_1), see Fig. 9**(a2)**. By contrast, extensive and severe states exhibit increased fragility due to shear key failure that prevents $P-\Delta$ effect development. At such H/d level, the development of pier fragility is similar across water depths, showing limited dependence on submergence when the wave heights are relatively low.

By contrast, girder fragility (Fig. 9**(b)**) is zero for all states at $S_a < 0.4$ g, but then rises to 0.58 and 0.78 for severe (LS_4) and slight (LS_1) damages, respectively. This again confirms the limited influences of individual tsunami after weak ground shaking despite the water depth level. However, the fragility increases significantly at higher S_a due to shear key failures. Here, girder fragility also shows an up-down trend with water depth, again reflecting the shift from pier collapse to girder dislocation due to the increasing tsunami impact in horizontal direction. Note that girder fragility exhibits inconsistent development with water depths despite prior seismic levels, and this can be illustrated by the change in immersed state of bridge girders. In this context, the effective flow velocity causing impacts to girders increases from zero at lower water depths, but then decreases with water depths given specified H/d values due to wave profiles. As a result, the severe-damage fragility of girders remains zero even at the maximum S_a, which coincides with the conditional fragility result in Fig. 7.

Seismic-tsunami fragility was also analyzed for the S_a baseline intensity, see Fig. 10. In this case, the slight-damage fragility of pier develops notably at low tsunami levels, underlining the strong influence of initial seismic damage. Other states increase gradually with both S_a and H/d, with merely slight changes observed for H/d. The fragility generally rises with H/d and peaks around 0.45, again owing to bi-directional tsunami loads and $P-\Delta$ effects. Notably, the fragility remains relatively stable for each damage, implying that the influence of wave height surpasses that of depth. Similar to Fig. 9, the fragility remains comparable at lower H/d, while higher H/d level also introduces an up–down pattern with depth. The peak fragility at d = 6 m and H/d = 0.7 can be attributed to combined push-compressive forces on deformed piers that causes typical second-order effects, while d = 13.5 m exhibits reduced fragility due to merely dominant horizontal forces.

The girder fragility (Fig. 10**(b)**) shows minimal sensitivity to depth at low H/d, with only slight increases as H/d grows. Peak fragility occurs in shallow depths for large H/d, suggesting decreasing horizontal tsunami forces as water level arises. Comparing pier and girder fragility reveals that, the increasing depth tends to reduce girder fragility but enhance pier fragility, with the largest reduction at d = 6 m aligning with significant pier fragility growth, see subplot **(a)**. Hence, the fragility pattern of isolated bridges differs from moment-resisting types that has consistent rising with both hazard levels [54]. This can be attributed to the limited force transfer from girders to piers, which depends on the strength of intermediate linkages.

The seismic-tsunami analysis again highlights the dominant fragility of pier compared to girders for the isolated bridge. Both girder and pier fragility exhibits higher sensitivity to spectrum and relative wave height levels but limited dependence on water depth. Further, isolated and second-order effects can critically shape the multi-hazard fragility pattern for isolated bridges.

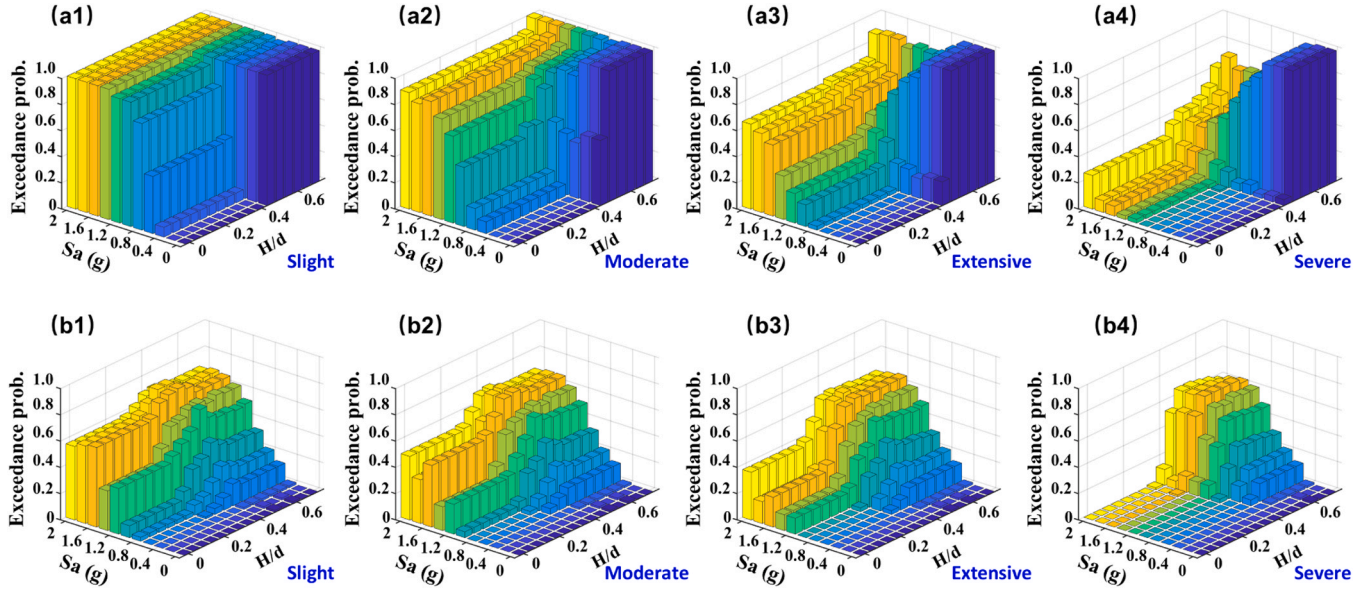

Fig. 8. Statistic seismic-tsunami fragility of primary components (d = 8.5 m): (a) pier; (b) girder.

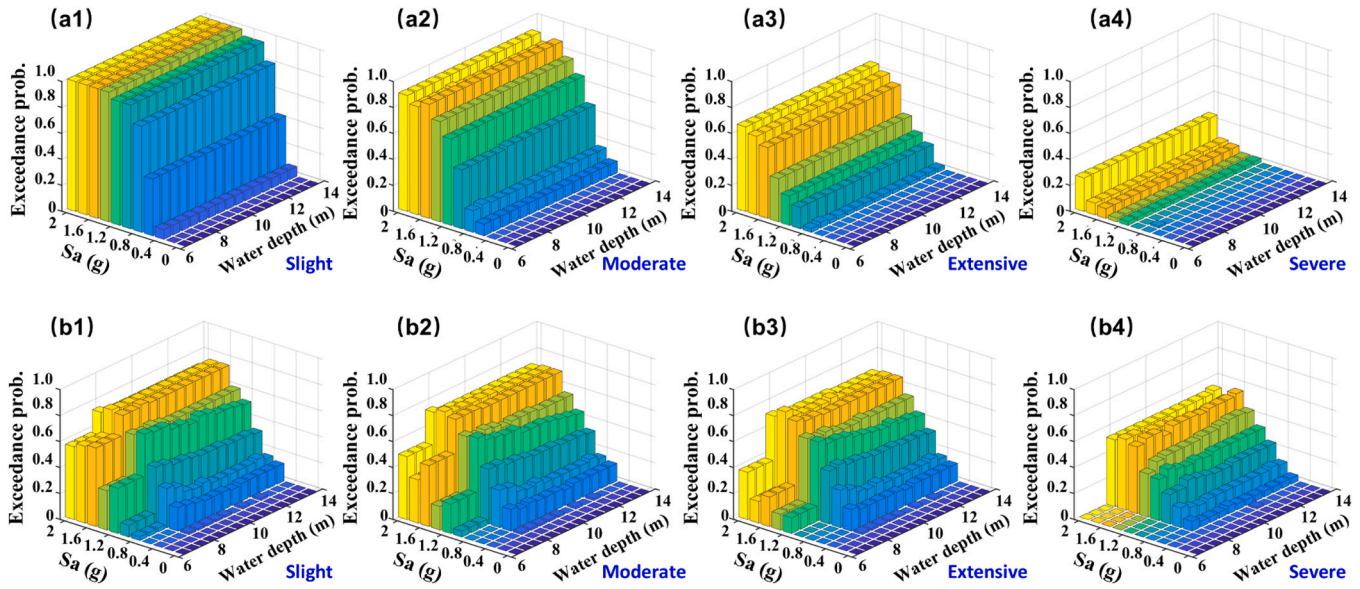

Fig. 9. Statistic seismic-tsunami fragility of primary components (H/d = 0.35): (a) pier; (b) girder.

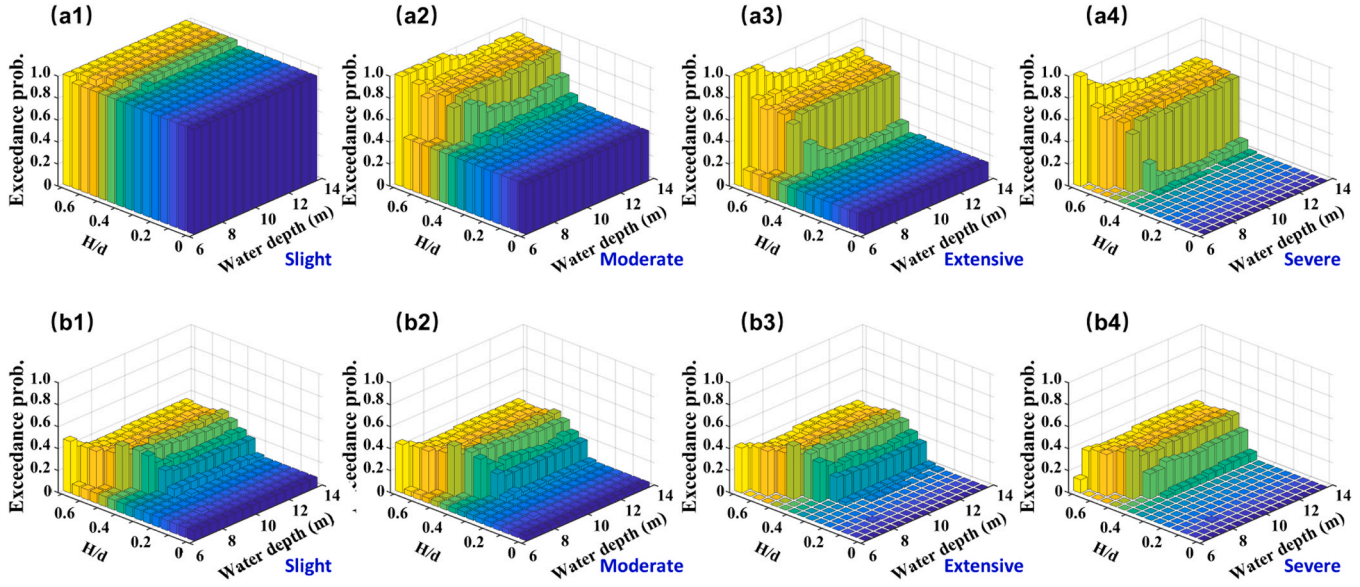

Fig. 10. Statistic seismic-tsunami fragility of primary components (S_a = 1.0 g): (a) pier; (b) girder.

4.2. *Analytical component-level fragility*

Following the statistical fragility analysis, analytical fragility was evaluated using vector-valued functions. Fig. 11–13 present the fragility of primary components under each baseline, with the first vector formula in Table 2 adopted and a fixed water depth at d = 8.5 m. The pier fragility rises with both S_a and H/d at the initial stage for all damage states, consistent with the statistical results in Fig. 8**(a)**. Fragility value of 1.0 is observed at the upper bound for slight damage (Fig. 11**(a1)**), whereas only at $S_a = 0$ g for other states. This reflects that shear key failure prevents the tsunami load transferred to piers, which then leads to reduced $P-\Delta$ effects. A minor drop in slight-damage fragility occurs near $S_a = 0.4$ g due to absent shear key limitations, coinciding with the statistic results in Fig. 8**(a1)**. For moderate damage, the fragility reaches unity at upper H/d at $S_a = 0$ g, but falls below unity at the coincident upper bounds. The major reason also lies in the reduced forces to piers after shear key failure, and similar pattern occurs also for extensive and severe damages **(a3–a4)**.

As can be seen in Fig. 11**(b)**, girder elements result in uniform fragility development. The fragility peaks near the coincident upper bound for all damages, indicating a direct contribution from both hazards. At lower S_a levels, fragility remains zero for all damages, suggesting again the limited influence of tsunami alone after minor earthquakes. Fragility at severe damage stays near zero across H/d while other states grow with S_a, implying the effect of initial seismic loading in amplifying tsunami damages, as seen in Fig. 11**(b4)**. Comparing different S_a indicates that, the fragility sensitivity to H/d develops directly as S_a increases.

Given a fixed H/d value at 0.35, the pier fragility shows monotonical growth with S_a, with minimal variation observed across water depths (Fig. 12**(a)**). This again addresses the dominant influence of wave height compared to water depth. And the maximum fragility of each damage shows good alignment with statistical results. Here, girder fragility develops consistently with S_a for LS_1~LS_3 across depths, while the severe-

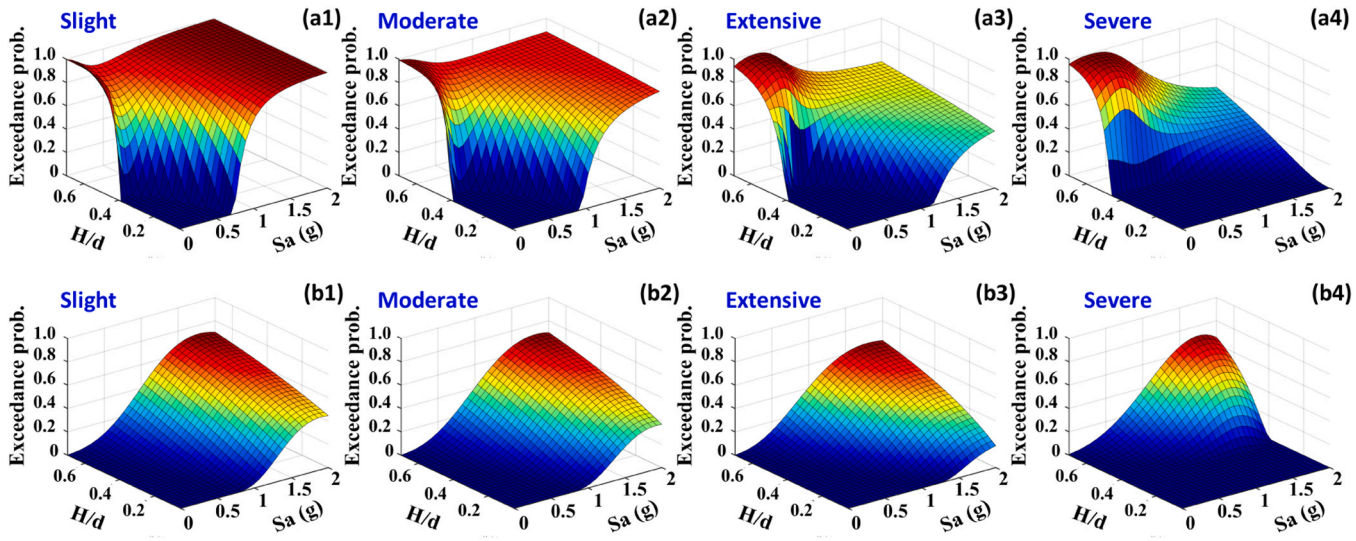

Fig. 11. Analytical seismic-tsunami fragility of primary components (d = 8.5 m, log-sum model): (a) pier; (b) girder.

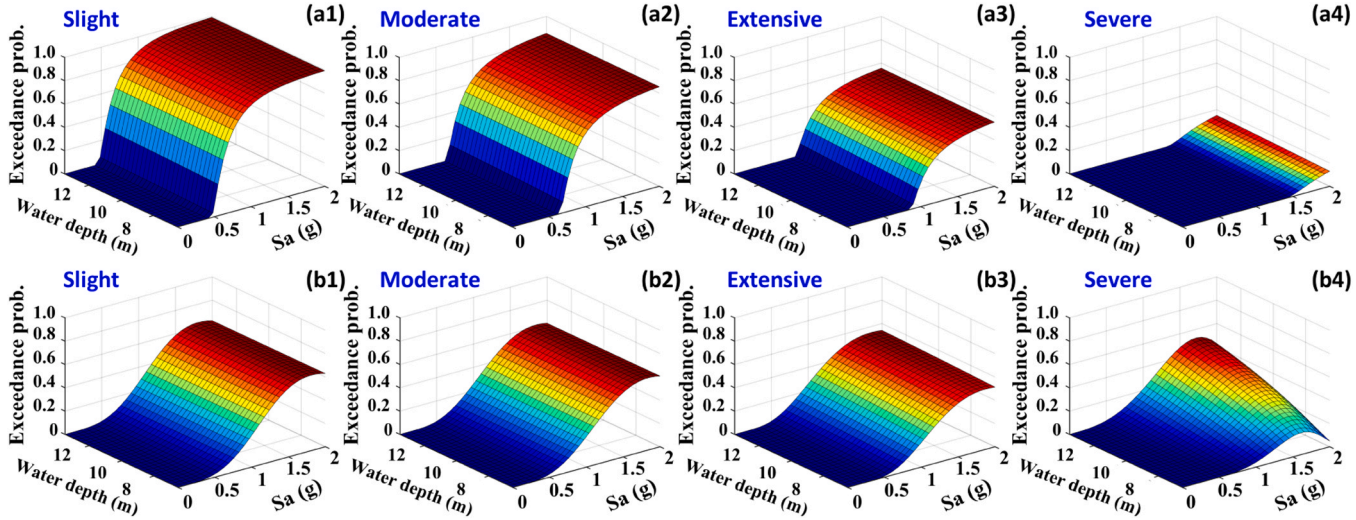

Fig. 12. Analytical seismic-tsunami fragility of primary components (H/d = 0.35, log-sum model): (a) pier; (b) girder.

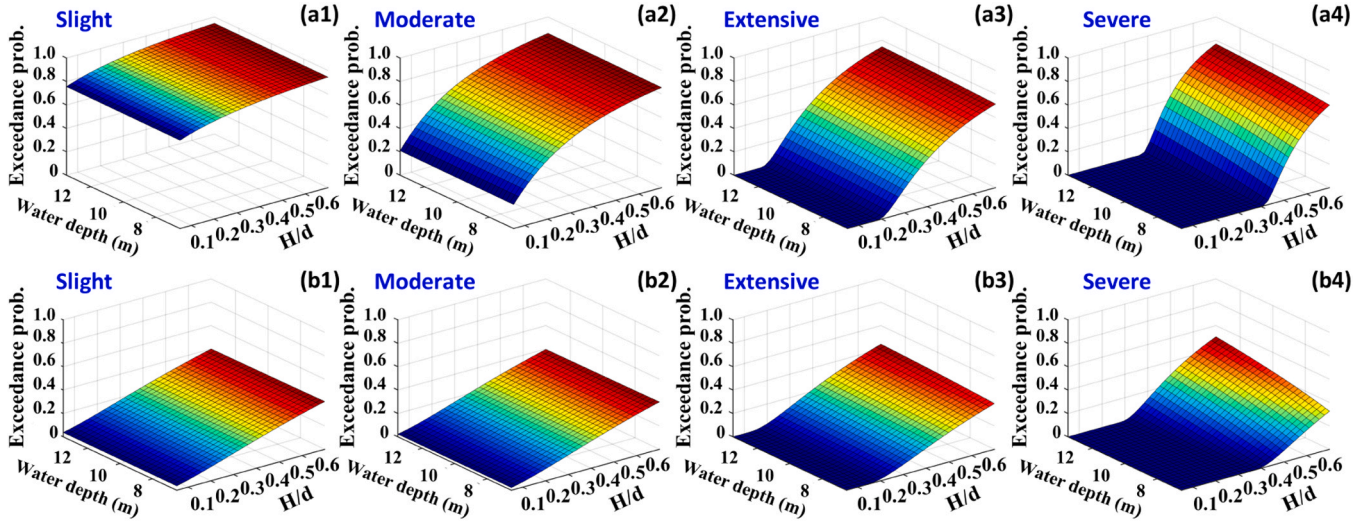

Fig. 13. Analytical seismic-tsunami fragility of primary components (S_a = 1.0 g, log-sum model): (a) pier; (b) girder.

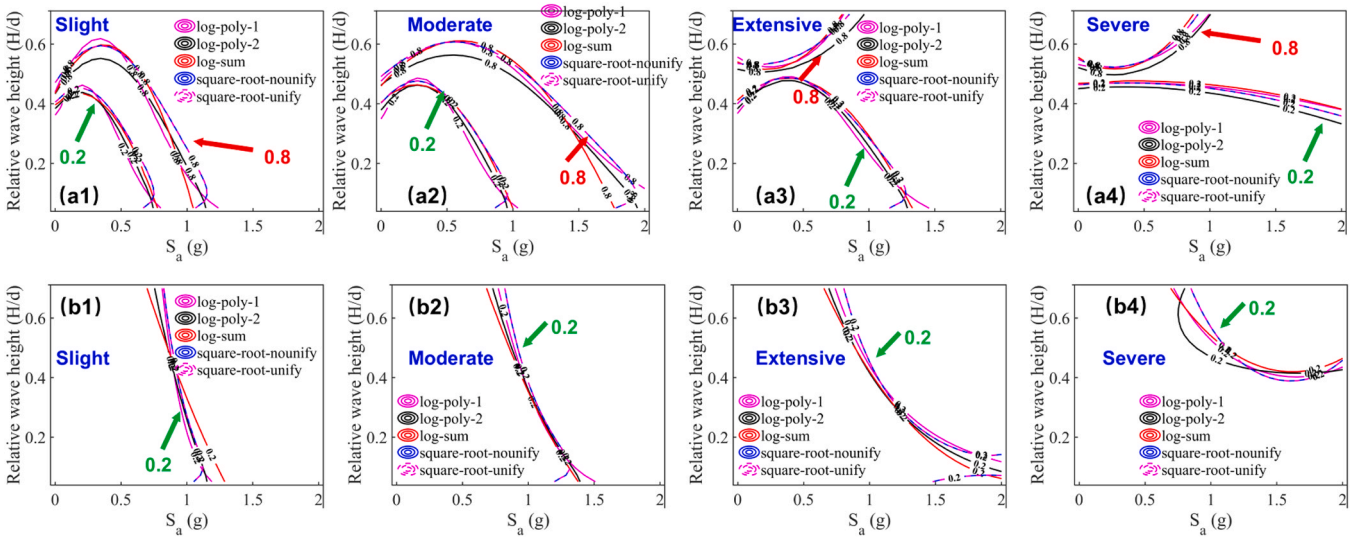

Fig. 14. Comparison of joint fragility from different vector-valued functions (d = 8.5 m): (a) pier; (b) girder.

damage fragility varies notably with water depths as seismic level rises, mirroring the up-down pattern in Fig. 9**(b4)**.

Fig. 13 further presents the fragility at fixed spectral level of 1.0 g. Herein, pier fragility exhibits steady increase with H/d across all states. Slight- and moderate-damage fragility remain above zero at the lowest tsunami level, indicating the notable influence of residential seismic damage. In contrast, extensive- and severe-damage fragility yields zero values in the same zone, aligning with the zero seismic fragility in Fig. 5 **(a)**. The variation with water depth is also minimal for LS_1~LS_3 but becomes pronounced for LS_4, see Fig. 13**(a4)**. Note that the statistic fragility varies notably with depth in Fig. 10, but the log-sum fragility model fails to capture such dependence, though it performs well in modeling H/d influence. In comparison, the girder fragility under such seismic levels remains near zero at lower H/d levels for extensive (LS_3) and severe (LS_4) states. Slight- and moderate-damage fragility develops almost linearly with H/d, while the fragility value at extensive and severe states approaches nonlinear trends with strong water depth sensitivity, see **(b3)** and **(b4)**. Comparing with statistic results suggest that vector-valued method tends to underestimates the peak fragility for spectral baselines.

The analytical fragility further confirms the coupled sensitivity of pier elements to seismic and tsunami intensities for isolated bridges, which mainly arises due to the tsunami loads in multiple directions. In this regard, the pier-linkage interaction alongside residual seismic damages can largely affect bridge responses under such sequential hazard actions.

4.3. Comparison of vector model effectiveness

To assess the effectiveness of different vector fragility models, their calculated results were compared in this section. To this regard, the contour plots at levels 0.2 and 0.8 were used, as seen in Figs. 14–16. For pier fragility estimation, the square-root model yields similar patterns for unified and non-unified formulas across damage states, indicating low sensitivity to their factor combination. In contrast, notable difference appears between the log-sum and log-poly-1 models. The log-poly-2 model matches other models at the 0.2 contour but produces higher fragility at 0.8, especially for LS_2 and above, as seen in **(a1)-(a2)**. The log-sum model gives intermediate results, while log-poly-1 predicts the lowest fragility at slight damage for $S_a < 0.5$ g. Notably, LS_3~LS_4

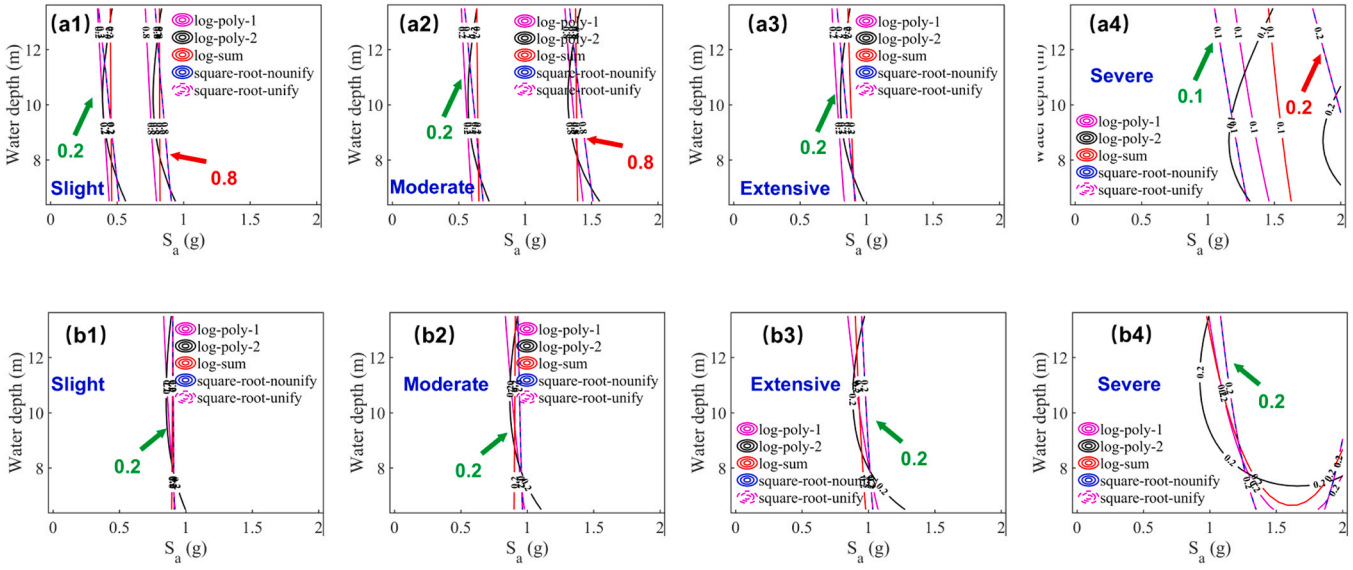

Fig. 15. Comparison of joint fragility from different vector-valued functions (H/d = 0.35): (a) pier; (b) girder.

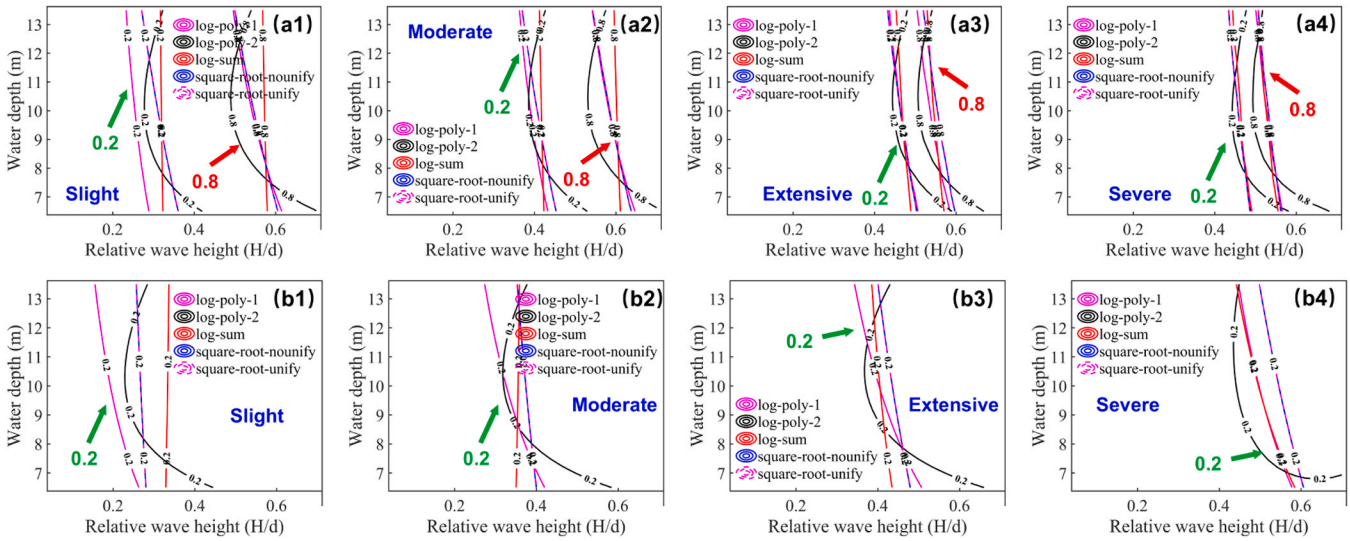

Fig. 16. Comparison of joint fragility from different vector-valued functions: (a) pier (0.5 g); (b) girder (1.0 g).

contours differ markedly from lower states (LS_1~LS_2) in its pattern, with maximum values at $S_a = 0$ and minimum at large S_a values. This aligns with the unique up-down fragility surface in Fig. 11, reflecting the strong tsunami actions when shear key failure is avoided during first earthquakes. The difference between models narrows for LS_3~LS_4, though log-poly-2 prediction remains the highest at 0.8 level, see Fig. 14 **(a3)**.

For girder elements, only the 0.2 contour level was shown as maximum fragility remains below 0.7 as per Fig. 8. In this case, the prediction shows similar development across models for LS_1~LS_3 states, see Fig. 14**(b1)-(b3)**. The square-root model diverges at $S_a = 1.5$–2.0 g for extensive state, suggesting overestimation at higher seismic intensities. LS_4 yields even greater disparity, where the log-poly-2 model gives the highest fragility, while the square-root model is lowest for $S_a < 1.2$ g. After that, the model distinction tends to decline with increasing spectral levels, showing their comparable capability under intensive ground motions. Therefore, log-poly-2 model is most conservative for a water depth (d) baseline, while square-root model yields the lowest values.

Fig. 15 indicates the contour result at fixed H/d = 0.35, in which 0.1 and 0.2 levels were specifically utilized for LS_4 state due to its limited fragility. It was found that square-root model again yields similar results despite unified factors. Limited model distinctions can be observed for LS_1~LS_3 states as opposed to LS_4 state, in which square-root and log-poly-2 models produce fragility above 0.2 while others remain below. In addition, log-poly-1 model yields the highest fragility for LS_1~LS_3 states, whereas square-root model dominants at LS_4. The lowest fragility was found with log-sum model at the 0.2 level, but is then altered by the square- root model at 0.8, see **(a1) and (a2)**. In this figure, the predicted LS_1~LS_3 fragility for girders also show minimal variation across models, but LS_4 result reveals notable differences around $S_a = 1.0$ g, with log-poly-2 model yielding the lowest outcome while log-poly-1 and square-root models exhibit jumping increases at $S_a = 1.3$–1.5 g.

Fig. 16 compares fragility at fixed $S_a = 0.5$ and 1.0 g for piers and girders, respectively. In this case, model differences become more significant than Figs. 14 and 15. Log-poly-1 model gives the largest prediction for LS_1 and LS_2 states at 0.2 contour, while LS_3 and LS_4 results converge, as seen in **(a3)-(a4)**. In this case, the log-sum model was found to produce the lowest fragility across all damage states, while log-poly-2 model yields a curved fragility trend that differs from the linear development in other models. For girder fragility, log-poly-1 provides the highest LS_1 prediction, while log-sum the lowest according to **(b1)**. In contrast, the square-root model produces the lowest results for LS_2~LS_4 states, while log-poly-2 yields the highest outcome for LS_4, indicating a potential conservative prediction on bridge fragility.

On this basis, the model fitting capacity was evaluated using Akaike Information Criterion (AIC), with errors in Table 4 weighted by the damage state importance, taking 0.10, 0.15, 0.25, 0.50 for LS_1~LS_4 in the current research. Herein, only pier and girder elements were addressed owing to their crucial role in bridge performance. It should be mentioned that the importance factor is hypothesized here but could be determined by bridge significance and functionality, which are beyond the scope of the present work. The result shows that log-sum model gives the smallest error for all states except LS_1, where log-poly-1 is lower. Weighted average errors ($\times 10^5$) are 2.44 for log-sum model and 1.97 for log-poly-1 model, while log-poly-2 and square-root are higher at 3.01 and 3.24, respectively. For girder elements, log-sum model exhibits the lowest average error (0.31), with polynomial models higher (0.49 and 1.29) and square-root highest (3.73). Errors for the square-root model are also identical for unified and non-unified cases, aligning with earlier contour analysis. It is then clear that vector-valued method can have different applicability to various bridge components.

Table 5 further compares weighted AIC values across vector-based models using weighted importance. Herein, the model complexity includes both polynomial function and vector model. The pier prediction error after weighting drops to 1.72 but is again larger than log-poly-1 model at 1.59. In contrast, the log-sum model error for girder increases slightly to 0.43, as compared to square-root model taking 4.73. This highlights an increased prediction error at lower damage level for bridge piers, and a reduced error subject to severe damages for girders. By averaging pier and girder results, log-sum model was found to induce the lowest AIC (1.07), followed closely by log-poly-2 model (1.12). Such findings further highlight the importance of selecting proper vector models for isolated bridges subjected to earthquake and tsunami loads. Among them the log-sum model provides balanced accuracy and stability across hazard baselines.

4.4. Assessment on system-level performance

Based on component-level fragility, system-level fragility was calculated using the upper bound of the SOLM estimation according to Section 2.2, and the log-sum model was employed due to their least errors.

4.4.1. System-level fragility

Fig. 17 presents the statistical result at each hazard baseline as in

Table 4
Comparison of prediction errors from various vector-valued functions.

Component	Function No.	Model errors ($\times 10^5$)					Rank
		Slight	Moderate	Extensive	Severe	Mean	
Pier	1	5.86	1.42	1.24	1.22	2.44	2
	2	3.40	1.77	1.47	1.24	1.97	1
	3	2.55	7.75	0.97	0.76	3.01	3
	4	2.65	2.79	3.22	4.32	3.24	4
	5	2.65	2.79	3.22	4.32	3.24	4
Girder	1	0.11	0.20	0.30	0.62	0.31	1
	2	0.29	0.30	0.38	0.97	0.49	2
	3	0.26	0.27	0.35	4.29	1.29	3
	4	2.24	2.79	3.44	6.46	3.73	4
	5	2.24	2.79	3.44	6.46	3.73	4

Table 5
Comparison of AIC outcomes from different vector-valued functions.

Vector-valued function	Model complexity	Model errors ($\times 10^5$)		AIC estimation ($\times 10^5$)	Rank
		Pier	Girder		
Log-sum	7	1.72	0.43	1.07	1
Log-poly-1	9	1.59	0.65	1.12	2
Log-poly-2	12	2.04	2.30	2.16	3
Square-root-nounify	9	3.65	4.73	4.19	4
Square-root-unify	8	3.65	4.73	4.19	5

Figs. 14–16. For both d and H/d baselines, fragility value remains at zero at the coincident lower bound for all damage states, see subplots **(a)-(b)**. In most cases, fragility increases steadily with both intensities but shows an up-down trend around H/d = 0.35, consistent with the girder fragility pattern in Fig. 9. Notably, the maximum system-level fragility reaches 1.0 while the component-level remains below, showing the contribution from various bridge components. As a result, severe-damage fragility approaches unity at the upper bound even when pier and girder fragility are far lower. This implies a significant failure probability of isolated bridge under such combined hazard impacts. At $S_a = 0.5$ g, fragility remains negligible at lower H/d for all water depths, showing again that tsunami alone have minimal impacts while without strong earthquakes occuring initially (Fig. 17**(c)**). Note that the 0.5-g ground motion intensity was used here to alter 1.0 g, as the latter fragility is near unity across all intensities.

Fig. 18 compares the statistical and analytical fragility in a system level. It can be found that, the fragility at lower seismic bound yields zero values for LS_2~LS_4 at small H/d values. Whereas, LS_1 fragility

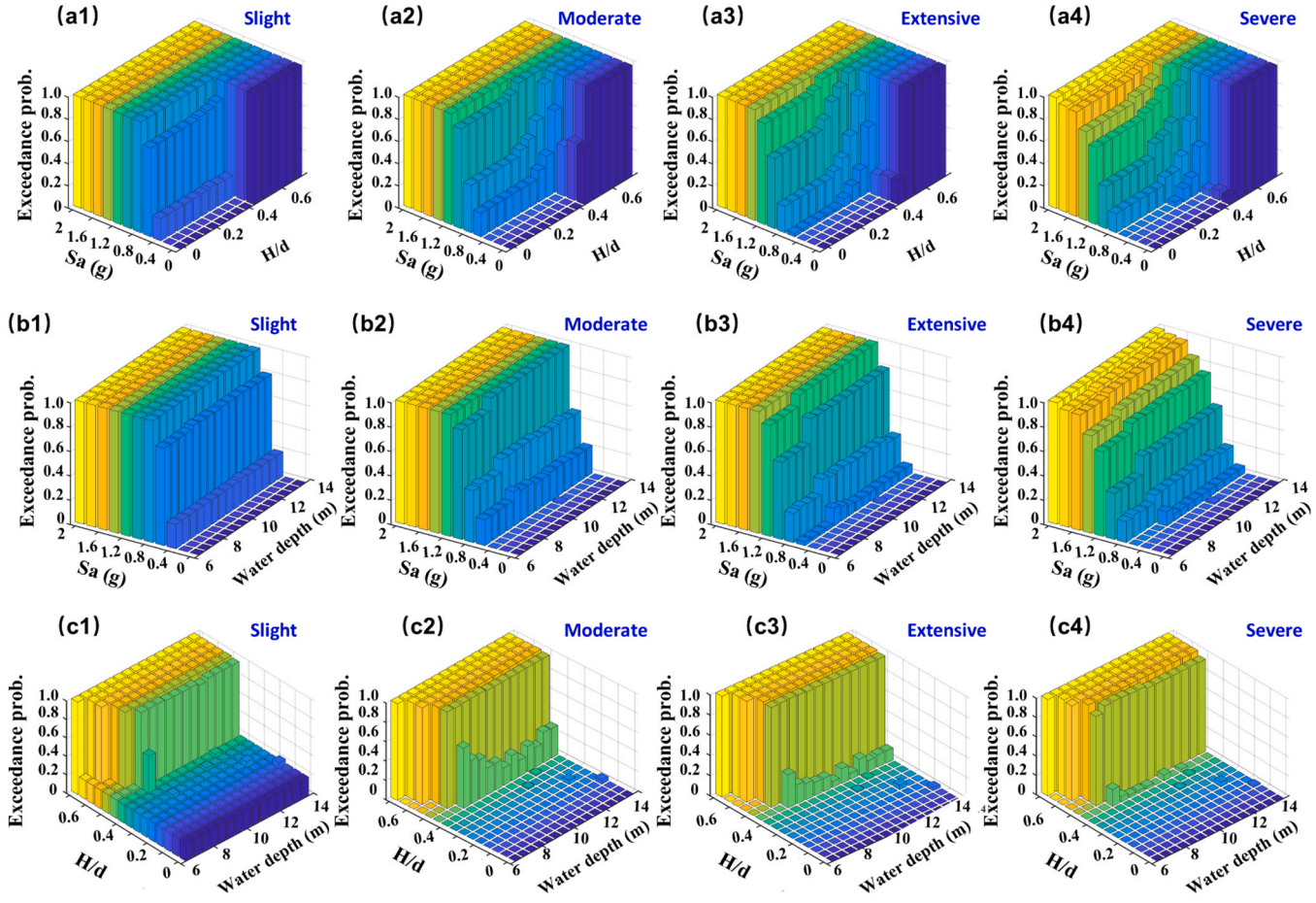

Fig. 17. Statistic seismic-tsunami fragility of bridge system: (a) d = 8.5 m; (b) H/d = 0.35; (c) $S_a = 0.5$ g.

shows non-zero initial values due to notable shear key fragility to horizontal tsunami forces even at $S_a = 0$ g, see Fig. 18**(a1)**. Note that this does not contradict Fig. 7, where marginal tsunami fragility remains zero before H/d = 0.45. This is because the marginal result only accounts for tsunami influence, while the joint fragility also includes complete prior seismic responses. Along the seismic intensity, LS_1 and LS_2 fragility exhibit a fall-rise trend (Fig. 18**(a1), (a2)**), while LS_3 and LS_4 follow an up-down-up pattern shown in **(a3)-(a4)**. This aligns with the pier fragility trend in Fig. 11, also owing to the enhanced $P-\Delta$ effects. In contrast, the sytem-level fragility increases monotonically with H/d for all states and spectrum levels, and this further underlines the dominant influence of wave height.

Analytical results at H/d = 0.35 show that fragility increases steadily with S_a, and then reaches unity even before the upper bound, see Fig. 18 **(b)**. Nevertheless, the value remains stable across water depths, showing good agreement with the limited sensitivity to depth. The fragility value is larger than zero even at $S_a = 0$ g because of shear key damage contributions. The fragility directly rises with H/d for all depths, followed by a sharp increase near H/d = 0.45, and this aligns with the conditional pier results in Fig. 7**(a)**. While fragility is nearly constant across depths for small H/d, depth effects become more evident when H/d value becomes larger, as seen in Fig. 18**(c3), (c4)**.

The comparison indicates a good agreement between statistical and analytical result under various hazard baselines. Under depth-based baseline, the component fragility aligns well with statistical results along both H/d and S_a. For H/d baselines, fragility rises quickly for slight damage but more gradually for severe damage, which is also consistent with statistic patterns. However, analytical predictions fail to capture the up-down trend with rising depth for moderate to severe states (Fig. 17**(b2), (b4)**). At specified S_a levels, analytical fragility can provide good prediction across damage states. Comparing the surface pattern of statistic and analytical methods, the log-sum model is suitable for estimating system-level fragility under S_a and H/d baselines but less effective for water-depth. Besides, this analysis also reveals that multi-component interactions tend to amplify overall bridge vulnerability. Further, the coupled hazard effects, along with component-level interdependence can largely affect the global performance of isolated bridges.

4.4.2. *Damage ratio analysis*

Additionally, the integrated influence of various damage states was examined using a damage ratio index, which is defined as the damage loss over construction cost, see Fig. 19. In this context, each damage state was designed with contribution to the integral damage of bridges, with truncated normal distribution to capture uncertainties. Following prior study on bridge loss assessment [55], the upper bound of truncated normal distribution was defined as 5 %, 15 %, 40 %, and 100 % for LS_1~LS_4 states, with lower found equal to 1 %, 2 %, 10 %, 30 %. The log-sum model results are adopted for fragility estimation, with the mean of each truncated model to reflect an expectation-level consequence. Therefore, the calculated damage ratio value must remain below unity across both hazard magnitudes.

The result in Fig. 19**(a)** shows that, damage ratio increases consistently with H/d, with higher initial value observed at H/d = 0 for larger S_a values. Given higher H/d levels (Fig. 19**(a)**), the damage ratio exhibits a down-up trend with S_a, aligning well with the system-level fragility in Fig. 18. Fig. 19**(b)** reveals that the damage ratio rises with S_a but shows negligible variation with depth at H/d = 0.35. Besides, the results at S_a = 0.5 g indicates a proportional ratio growth with H/d, with significant variation observed for H/d > 0.45, see Fig. 19**(c)**. Notably, the initial values above zero again highlight the role of prior damage due to ground shakings. The maximum damage ratio is about 0.65 for all baselines, which exactly corresponds to the mean damage ratio of LS_4 state. This highlights the dominating effects of severe damage at the upper bound intensity, compared to the limited contribution from low-level damage states. Hence, both relative wave height (H/d) and spectrum level (S_a)

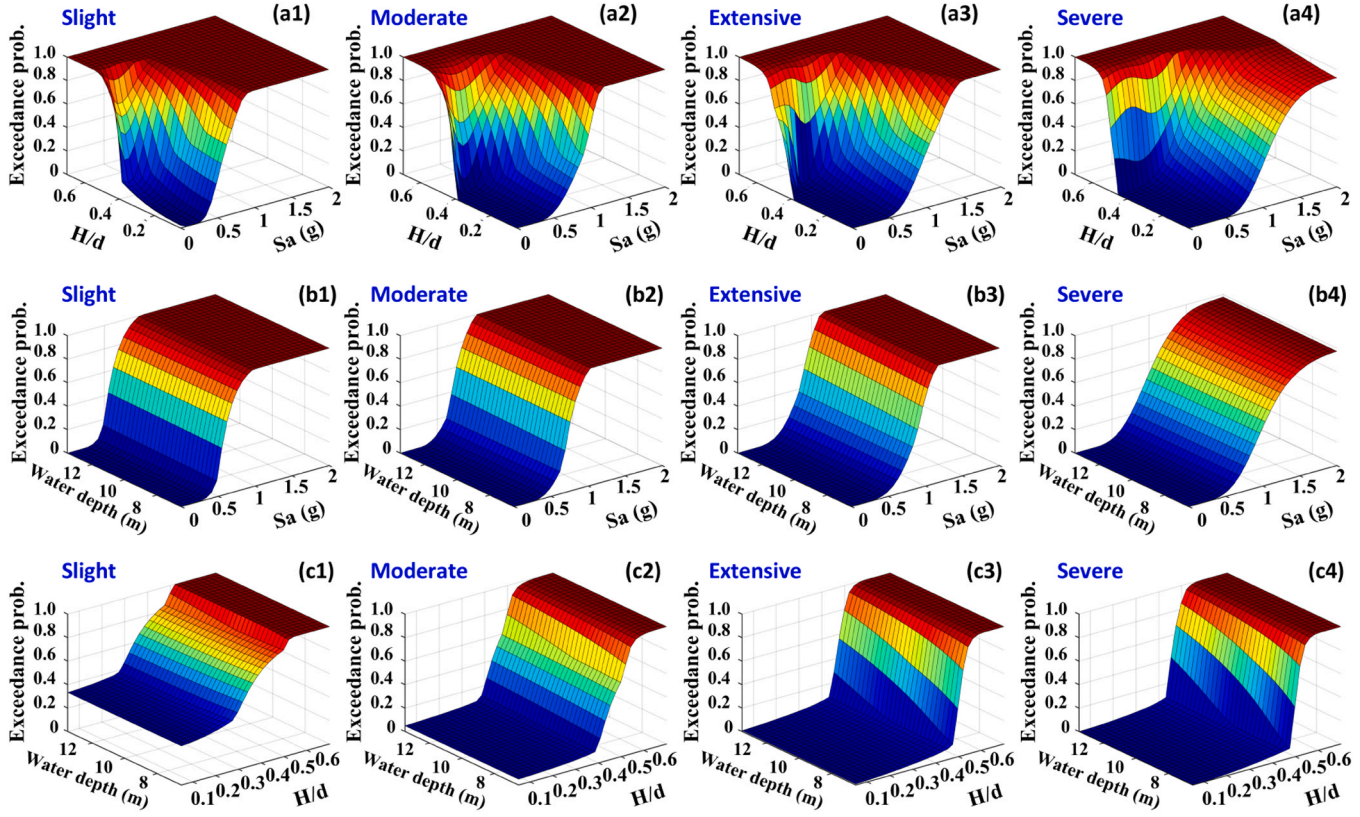

Fig. 18. Analytical seismic-tsunami fragility of bridge system (function I): (a) d = 8.5 m; (b) H/d = 0.35; (c) S_a = 0.5 g.

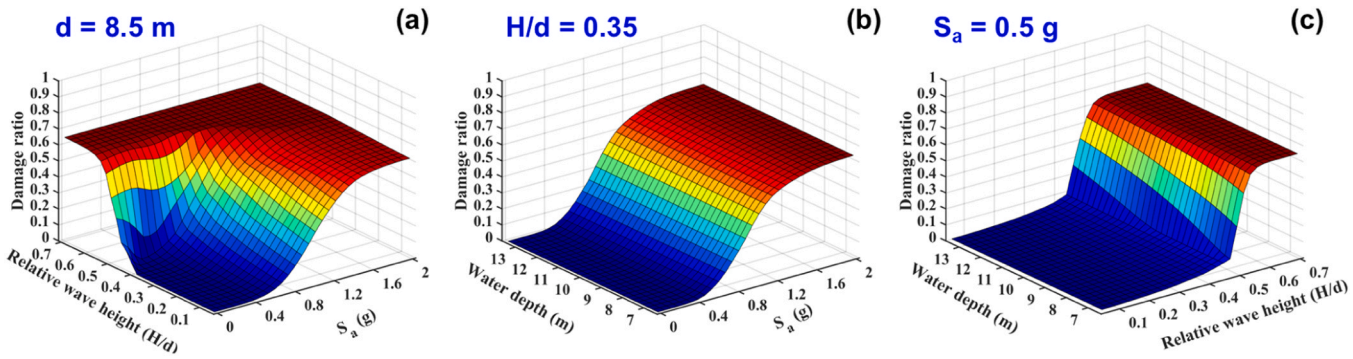

Fig. 19. Vulnerability of isolated bridge in terms of average damage ratio versus hazard intensity: (a) d = 8.5 m; (b) H/d = 0.35; (c) S_a = 0.5 g.

can largely affect damage ratios, leading to consistent increases with each hazard intensity and peaks over their upper bounds. In contrast, water depth exhibits little contributions under lower H/d, regardless of prior seismic intensities.

5. Conclusion

In this study, the performance of isolated bridges under earthquake and tsunami hazards was assessed via a fragility-based framework. Multi-hazard intensities were defined according to physical mechanisms, with a single measure adopted for earthquake and bi-variates measures for tsunamis. Analytical fragility was assessed via various vector-valued models, with system-level fragility derived from SOLM approach. Further, damage ratios were estimated to yield quantitative description of hazard consequences.

The primary contributions and findings of this study are summarized as follows:

(1) Isolated bridge has distinct seismic fragility from integral bridges due to the strength of linkage elements relative to piers. Pier fragility increases before extremely large seismic magnitudes while girder fragility develops inconsistently with seismic levels.
(2) The seismic-tsunami fragility of piers grows directly with relative wave heights, but decreases with seismic intensity under higher H/d levels, while girder fragility yields an up-down development with both hazard intensities.
(3) Log-sum model yields the best fitting capability, with square-root model the worst. Vector-valued method can estimate the fragility of major bridge components but tends to underestimates for H/d baselines.
(4) Spectrum acceleration and relative wave height have dominant influences on isolated bridge fragility, as opposed to the limited impact from water depths.
(5) Log-sum fragility function can be further employed for the risk assessment of isolated bridge under sequential seismic-tsunami actions.

Limitations and prospects

(1) This study only considered structural uncertainty in geometry and strength. Further research is demanded with respect to random tsunami forces.
(2) The current work only adopts a single design for linkage element. A parametric study with different linkage designs is vital to evaluate their influences.
(3) Vector-valued function has limited accuracy in estimating system-level fragility. Alternative methods such as generalized linear estimation (GLE) merit investigation in the future.
(4) Weight factors for AIC evaluation are assumed in this study. Further studies should refine these factors by considering their contribution to global bridge functionality.

CRediT authorship contribution statement

Anxin Guo: Writing – review & editing, Supervision, Funding acquisition. **Frangopol Dan M.:** Writing – review & editing, Supervision. **Heng Mei:** Writing – original draft, Methodology, Formal analysis, Conceptualization. **You Dong:** Writing – review & editing, Supervision, Funding acquisition.

Declaration of Competing Interest

All authors disclosed no relevant relationships.

Acknowledgements

The presented research is greatly sponsored by the Environment and Conservation Fund (No. ECF 42/2022), HKSAR, China, and the ANR/RGC Joint Research Scheme (No. A-PolyU502/23) , HKSAR, China, the National Natural Science Foundation of China (52595691, 52438009), Fundamental Research Funds for the Central Universities (FRFCU5710093320), Heilongjiang Touyan Innovation Program Team. The authors would like to show great appreciation to all the sponsors above.

Data availability

Data will be made available on request.

References

[1] Yashinsky M., Oviedo R., Ashford S., GabaldonL F., Hube M.. Performance of highway and railway structures during the February 27, 2010 Maule Chile earthquake. EERI/PEER FHWA Bridge Team Report. 2010.
[2] Kawashima K, Unjoh S, Hoshikuma J, Kosa K. Damage of bridges due to the 2010 Maule, Chile, earthquake. J Earthq Eng 2011;15:1036–68.
[3] Scawthorn C., Porter K.A., Risk S.. Aspects of the 11 March 2011 Eastern Japan Earthquake and Tsunami. Reconnaissance Report. 2011.
[4] Wilches J, Santa María H, Riddell R, Arrate C. Influence of the use of external shear keys on the seismic behavior of Chilean highway bridges. Eng Struct 2017;147:613–24.
[5] Wilches J, Santa María H, Riddell R, Arrate C. Effects of changes in seismic design criteria in the transverse and vertical response of Chilean highway bridges. Eng Struct 2019;191:370–85.
[6] Frangopol DM, Dong Y, Sabatino S. Bridge life-cycle performance and cost: analysis, prediction, optimisation and decision-making. Struct Infrastruct Eng 2017;13:1239–57.
[7] Akiyama M, Frangopol DM, Ishibashi H. Toward life-cycle reliability-, risk- and resilience-based design and assessment of bridges and bridge networks under independent and interacting hazards: emphasis on earthquake, tsunami and corrosion. Struct Infrastruct Eng 2019;16:26–50.
[8] Ishibashi H, Akiyama M, Frangopol DM, Koshimura S, Kojima T, Nanami K. Framework for estimating the risk and resilience of road networks with bridges and

embankments under both seismic and tsunami hazards. Struct Infrastruct Eng 2020;17:494–514.
[9] Ishibashi H, Kojima T, Nanami K, Akiyama M, Frangopol DM. Risk estimation of bridges and bridge networks under seismic and subsequent tsunami hazards. EASEC16: Proceedings of The 16th East Asian-Pacific Conference on Structural Engineering and Construction, 2021. Springer; 2019. p. 1189–94.
[10] Ishibashi H., Kojima T., Akiyama M., Frangopol D.M., Koshimura S. A procedure for estimating the risk and resilience of bridge networks under both seismic and tsunami hazards. Bridge Maintenance, Safety, Management, Life-Cycle Sustainability and Innovations: CRC Press; 2021. p. 2101-2107.
[11] Padgett J.E. Sensitivity of Seismic Response and Fragility to Parameter Uncertainty. 2007.
[12] Ataei N, Padgett JE. Fragility surrogate models for coastal bridges in hurricane prone zones. Eng Struct 2015;103:203–13.
[13] Gehl P, Seyedi DM, Douglas J. Vector-valued fragility functions for seismic risk evaluation. Bull Earthq Eng 2013;11:365–84.
[14] Alam MS, Barbosa AR, Scott MH, Cox DT, van de Lindt JW. Development of physics-based tsunami fragility functions considering structural member failures. J Struct Eng 2018:144.
[15] Jafarian Y, Lashgari A, Miraiei M. Multivariate fragility functions for seismic landslide hazard assessment. J Earthq Eng 2021;25:579–96.
[16] Jafarian Y, Miraei M. Scalar- and vector-valued fragility Analyses of gravity quay wall on liquefiable soil: example of Kobe port. Int J Geomech 2019;19:04019029.
[17] Del Zoppo M, Rossetto T, Di Ludovico M, Prota A. Effect of buoyancy loads on the tsunami fragility of existing reinforced concrete frames including consideration of blow-out slabs. Sci Rep 2023;13:9015.
[18] Guo A, Yuan W, Lan C, Guan X, Li H. Time-dependent seismic demand and fragility of deteriorating bridges for their residual service life. Bull Earthq Eng 2015;13:2389–409.
[19] Guo X, Wu Y, Guo Y. Time-dependent seismic fragility analysis of bridge systems under scour hazard and earthquake loads. Eng Struct 2016;121:52–60.
[20] Li T, Lin J, Liu J. Analysis of time-dependent seismic fragility of the offshore bridge under the action of scour and chloride ion corrosion. Structures 2020;28:1785–801.
[21] Argyroudis SA, Mitoulis SA, Winter MG, Kaynia AM. Fragility of transport assets exposed to multiple hazards: state-of-the-art review toward infrastructural resilience. Reliab Eng Syst Saf 2019;191:106567.
[22] Guo X, Badroddin M, Chen Z. Scour-dependent empirical fragility modelling of bridge structures under earthquakes. Adv Struct Eng 2018;22:1384–98.
[23] Mei H, Guo A. Seismic-tsunami fragility analysis for box-girder simple-support bridge with transverse RC constrainers. Ocean Eng 2024;304:117578.
[24] Pang Y, Meng R, Li C, Li C. A probabilistic approach for performance-based assessment of highway bridges under post-earthquake induced landslides. Soil Dyn Earthq Eng 2022:155.
[25] Hu H, Fu C, Bao Y, Liu L, Shi S, Zhu F, et al. Seismic fragility assessment of slopes with scalar-valued and vector-valued earthquake intensity measures. Acta Geotech 2025:1–16.
[26] Guo Z, Han J, El Naggar MH, Bi Y, Xu C, Du X. Vector-valued fragility analysis of subway station structures subjected to the Kahramanmaras earthquake. Soil Dyn Earthq Eng 2024;182:108739.
[27] Bojórquez E, Iervolino I, Reyes-Salazar A, Ruiz SE. Comparing vector-valued intensity measures for fragility analysis of steel frames in the case of narrow-band ground motions. Eng Struct 2012;45:472–80.
[28] Mei H, Quek ST, Guo A. Seismic-tsunami risk assessment for isolated coastal bridges using nested Copula method. Eng Struct 2025;328:119715.
[29] Zhu D, Dong Y, Feng R, Li Y, Zhai C. Dynamic responses and cumulative damage of coastal bridges subjected to extreme sequential earthquake-tsunamis. Soil Dyn Earthq Eng 2024;187:108975.
[30] Muntasir Billah AHM, Shahria Alam M. Seismic fragility assessment of highway bridges: a state-of-the-art review. Struct Infrastruct Eng 2014;11:804–32.
[31] Subcommittee on Bridges SS, and Transportation Officials. Subcommittee on Bridges. Guide specifications for seismic isolation design: AASHTO; 2010.
[32] Yim SC, Boon-Intra S, Nimmala SB, Winston HM, Azadbakht M, Cheung KF. Development of a guideline for estimating tsunami forces On bridge superstructures. Oregon. Dept Transp Res Sect 2011.
[33] McCowan JVII. On the solitary wave. Lond Edinb Dublin Philos Mag J Sci 1891;32:45–58.
[34] Mei H, Guo A. Toward the response of coastal bridges with updated RC shear key properties under the multi-hazard action of earthquakes and tsunamis. Ocean Eng 2024;297:117048.
[35] Campbell KW, Bozorgnia Y. NGA-West2 ground motion model for the average horizontal components of PGA, PGV, and 5% damped linear acceleration response spectra. Earthq Spectra 2014;30:1087–115.
[36] Reid JA, Mooney WD. Tsunami occurrence 1900–2020: A global review, with examples from Indonesia. Pure. Appl Geophys 2023;180:1549–71.
[37] Hayashi Y. Empirical relationship of tsunami height between offshore and coastal stations. Earth Planets Space 2010;62:269–75.
[38] Bryant N. Analytical Fragility Curves for Highway Bridges in Moderate Seismic Zones 2005.
[39] Siqueira GH, Sanda AS, Paultre P, Padgett JE. Fragility curves for isolated bridges in eastern Canada using experimental results. Eng Struct 2014;74:311–24.
[40] Zhang C, Zhao M, Zhong Z, Du X. Seismic intensity measures and fragility analysis for subway stations subjected to near-fault ground motions with velocity pulses. J Earthq Eng 2022;26:8724–50.
[41] Zakeri B, Padgett JE, Amiri GG. Fragility analysis of skewed single-frame concrete box-girder bridges. J Perform Constr Facil 2014;28:571–82.
[42] Modica A, Stafford PJ. Vector fragility surfaces for reinforced concrete frames in Europe. Bull Earthq Eng 2014;12:1725–53.
[43] Yan J, Guo A, Li H. Comparative analysis of different types of damage indexes of coastal bridges based on time-varying seismic fragility. Mar Struct 2022;86:103288.
[44] Mei H, Guo A. Quasi-static experimental study on seismic performance of exterior shear key with different failure modes. Eng Struct 2023;287:116173.
[45] Baker JW, Lee C. An improved algorithm for selecting ground motions to match a conditional spectrum. J Earthq Eng 2018;22:708–23.
[46] Huang B, Duan L, Yang Z, Zhang J, Kang A, Zhu B. Tsunami forces on a coastal bridge deck with a box girder. J Bridge Eng 2019;24:04019091.
[47] Morison J, Johnson JW, Schaaf SA. The force exerted by surface waves on piles. J Pet Technol 1950;2:149–54.
[48] Zhu D, Dong Y. Experimental and 3D numerical investigation of solitary wave forces on coastal bridges. Ocean Eng 2020;209:107499.
[49] Zhu D, Dong Y, Frangopol DM. Experimental and numerical investigation on wave impacts on box-girder bridges. Struct Infrastruct Eng 2022;18:1379–97.
[50] Chen M, Huang B, Yang Z, Liao L, Zhou J, Ren Q, et al. Study on the mechanical characteristics and failure mechanism of the coastal bridge with a box-girder superstructure under the action of breaking solitary waves. Ocean Eng 2023;287:115834.
[51] Mander JB, Priestley MJ, Park R. Theoretical stress-strain model for confined concrete. J Struct Eng 1988;114:1804–26.
[52] AASHTO. AASHTO LRFD bridge design specifications, customary U.S. units. Washington, DC: American Association of State Highway and Transportation Officials; 2012.
[53] Nielson BG, DesRoches R. Seismic performance assessment of simply supported and continuous multispan concrete girder highway bridges. J Bridge Eng 2007;12:611–20.
[54] Xu J, Wu G, Feng D, Fan J. Probabilistic multi-hazard fragility analysis of RC bridges under earthquake-tsunami sequential events. Eng Struct 2021:238.
[55] Burns PO, Barbosa AR, Olsen MJ, Wang H. Multihazard damage and loss assessment of bridges in a highway network subjected to earthquake and tsunami hazards. Nat Hazards Rev 2021;22:05021002.